



# Survey of Gravitationally Lensed Objects in HSC Imaging (SuGOHI). II. Environments and Line-of-Sight Structure of Strong Gravitational Lens Galaxies to $z \sim 0.8$

Kenneth C. Wong<sup>1,14</sup>, Alessandro Sonnenfeld<sup>2</sup>, James H. H. Chan<sup>3,4,5</sup>, Cristian E. Rusu<sup>6,15</sup>, Masayuki Tanaka<sup>1</sup>, Anton T. Jaelani<sup>7</sup>, Chien-Hsiu Lee<sup>6</sup>, Anupreeta More<sup>2,8</sup>, Masamune Oguri<sup>2,9,10</sup>, Sherry H. Suyu<sup>5,11,12</sup>, and Yutaka Komiyama<sup>1,13</sup>

<sup>1</sup> National Astronomical Observatory of Japan, 2-21-1 Osawa, Mitaka, Tokyo 181-8588, Japan

<sup>2</sup> Kavli IPMU (WPI), UTIAS, The University of Tokyo, Kashiwa, Chiba 277-8583, Japan

<sup>3</sup> Laboratoire d’Astrophysique, Ecole Polytechnique Fédérale de Lausanne (EPFL), Observatoire de Sauverny, CH-1290 Versoix, Switzerland

<sup>4</sup> Department of Physics, National Taiwan University, Taipei 10617, Taiwan

<sup>5</sup> Institute of Astronomy and Astrophysics, Academia Sinica, 11F of ASMAB, No.1, Section 4, Roosevelt Road, Taipei 10617, Taiwan

<sup>6</sup> Subaru Telescope, National Astronomical Observatory of Japan, 650 N Aohoku Pl., Hilo, HI 96720, USA

<sup>7</sup> Graduate School of Science, Tohoku University, 980-8578, 6-3 Aramaki Aoba, Aoba-ku, Sendai, Miyagi, Japan

<sup>8</sup> Inter-University Centre for Astronomy and Astrophysics, Post Bag 4, Ganeshkhind, Pune 411 007, India

<sup>9</sup> Department of Physics, The University of Tokyo, 7-3-1 Hongo, Bunkyo-ku, Tokyo 113-0033, Japan

<sup>10</sup> Research Center for the Early Universe, University of Tokyo, Tokyo 113-0033, Japan

<sup>11</sup> Max-Planck-Institut für Astrophysik, Karl-Schwarzschild-Str. 1, D-85748 Garching, Germany

<sup>12</sup> Physik-Department, Technische Universität München, James-Franck-Straße 1, D-85748 Garching, Germany

<sup>13</sup> Department of Astronomy, School of Science, Graduate University for Advanced Studies (SOKENDAI), 2-21-1 Osawa, Mitaka, Tokyo 181-8588, Japan

Received 2018 July 16; revised 2018 August 30; accepted 2018 September 19; published 2018 November 5

## Abstract

We investigate the local and line-of-sight (LOS) overdensities of strong gravitational lens galaxies using wide-area multiband imaging from the Hyper Suprime-Cam Subaru Strategic Program. We present 41 new definite or probable lens candidates discovered in Data Release 2 of the survey. Using a combined sample of 87 galaxy-scale lenses out to a lens redshift of  $z_L \sim 0.8$ , we compare galaxy number counts in LOSs toward known and newly discovered lenses in the survey to those of a control sample consisting of random LOSs. We also compare the local overdensity of lens galaxies to a sample of “twin” galaxies that have similar redshift and velocity dispersion to test whether lenses lie in different environments from similar nonlens galaxies. We find that lens fields contain higher number counts of galaxies compared to the control fields, but this effect arises from the local environment of the lens. Once galaxies in the lens plane are removed, the lens LOSs are consistent with the control sample. The local environments of the lenses are overdense compared to the control sample, and are slightly overdense compared to those of the twin sample, although the significance is marginal. There is no significant evidence of the evolution of the local overdensity of lens environments with redshift.

**Key words:** gravitational lensing: strong – large-scale structure of universe

## 1. Introduction

Strong gravitational lensing is a useful tool for studying the distribution of matter in the universe. The lensing effect arises from the total mass distribution along the line of sight (LOS)—including both baryonic and dark matter—and is generally dominated by the primary lensing mass. Thus, lensing is a unique probe of the mass structure of lens galaxies (e.g., Treu et al. 2006; Koopmans et al. 2009; Auger et al. 2010; Sonnenfeld et al. 2013b). Strongly lensed quasars can also be used to probe the Hubble constant ( $H_0$ ) through a measurement of their time delays (Refsdal 1964), independent of and complementary to other probes such as the cosmological distance ladder (e.g., Freedman et al. 2012; Riess et al. 2016). The latest constraints from time-delay lenses (Bonvin et al. 2017; Suyu et al. 2017; Wong et al. 2017b) show a higher  $H_0$  value than *Planck* CMB measurements, highlighting the importance of this independent probe.

However, lenses do not exist in isolation, but are embedded within the large-scale structure of the universe, including both the local lens environment and uncorrelated structure in projection. The lensing signal is perturbed by the integrated

effect of the LOS mass distribution from the observer back to the source redshift,  $z_S$ . Most of these perturbations are small and can be either ignored or approximated as a tidal perturbation (see McCully et al. 2017), but the presence of significant perturbers such as groups and clusters (e.g., Momcheva et al. 2006; Wong et al. 2011; Wilson et al. 2016, 2017; Sluse et al. 2017) or the combined effect of multiple perturbers can lead to biases in lens modeling if unaccounted for.

If strong lenses are randomly distributed on the sky, these effects should average out over a sufficiently large sample. On the other hand, these LOS structures could potentially boost the lensing efficiency and cause lenses to lie along biased LOSs (e.g., Oguri et al. 2005). In addition, the mass surface density of perturbers along the LOS, which we refer to as external convergence ( $\kappa_{\text{ext}}$ ), is unconstrained from lens modeling due to the mass-sheet degeneracy (e.g., Falco et al. 1985; Gorenstein et al. 1988; Saha 2000; Schneider & Sluse 2013; Xu et al. 2016).  $\kappa_{\text{ext}}$  does not average out, but instead leads to a bias on the inferred  $H_0$  from time-delay lensed quasars if unaccounted for (e.g., Collett et al. 2013; Greene et al. 2013; McCully et al. 2014, 2017).

In order to use strong lens galaxies to infer the generic properties of typical galaxies, it is necessary to ascertain

<sup>14</sup> EACOA Fellow.

<sup>15</sup> Subaru Fellow.

whether or not lenses are in unbiased LOSs and have environments that are representative of the underlying galaxy population. The Sloan Lens ACS Survey (SLACS; Bolton et al. 2006) studied over 100 galaxy-scale strong lenses and found that their structural properties are consistent with that of similar early-type nonlens galaxies (Bolton et al. 2008) and reside in similar local environments (Treu et al. 2009). However, the SLACS sample is primarily at low redshift ( $z_L \sim 0.2$ ) and is selected through spectroscopic identification of background sources. It is not known whether this holds true for lenses selected by broadband imaging at higher redshifts, where the clustering and bias properties of galaxies may differ from those selected by SLACS.

Using *Hubble Space Telescope* (*HST*) imaging, Fassnacht et al. (2011) studied the LOSs toward 20 known strong-lens galaxies, using galaxy number counts to evaluate the LOS overdensity relative to a control sample of randomly chosen LOSs. This study found that the LOS toward lenses tends to be overdense, but much of this effect arises from the local environment of the lens galaxies, which are biased toward massive elliptical galaxies and are known to cluster (e.g., Dressler 1980). Once the local lens environment is corrected for, the relative densities of the lens LOS are not significantly different from the random sample, which is consistent with results from cosmological simulations (Hilbert et al. 2007). However, this study had several limitations, including the small sample size of lenses and the relatively small field of view of the *HST* Advanced Camera for Surveys, which only allowed for a maximum aperture radius of 45'' over which to evaluate the LOS. In addition, there were uncertainties arising from cosmic variance due to a small control sample of truly random fields, as a larger contiguous control field was itself found to be biased. Furthermore, this study lacked galaxy redshifts to distinguish the contribution of the local lens environment from projected structure along the LOS, instead relying on a statistical correction based on galaxy clustering results.

Using deep multiband imaging data from the ongoing Hyper Suprime Cam Subaru Strategic Program (HSC SSP; Aihara et al. 2018b), we have recently discovered dozens of new gravitational lenses as part of the Survey of Gravitationally lensed Objects in HSC Imaging (SuGOHI; Sonnenfeld et al. 2018) project. With the sample of SuGOHI galaxy-scale lenses (hereafter “SuGOHI-g”), we use the high-quality imaging from the HSC SSP to overcome the technical limitations of the Fassnacht et al. (2011) analysis and study LOSs toward strong lenses in much more detail than has been possible in the past. The deep multiband imaging provides accurate photometric redshifts (Tanaka et al. 2018) for distinguishing galaxies in the local lens environment from those projected along the LOS. In addition, the SuGOHI-g sample includes lenses up to  $z \sim 0.8$ , allowing us to study lens environments to higher redshifts than was previously possible with the SLACS sample, and to compare them to nonlens galaxies of similar redshift and mass. Finally, detailed analyses of individual SuGOHI-g lenses may require ancillary data, and it will be useful to consider which lenses are likely to be impacted by overdense environments or LOSs when deciding which systems to prioritize for such follow-up observations.

This paper is organized as follows. We describe the HSC SSP imaging data and BOSS spectroscopic data used in this study in Section 2. In Section 3, we present newly discovered lens candidates in Data Release 2 of the HSC SSP. We describe

our sample selection of lenses for this study, as well as our selection of twin galaxies and control fields in Section 4. In Section 5, we describe our methodology for calculating the density of the local environment and the LOS. We present our main results in Section 6 and summarize our conclusions in Section 7. Throughout this paper, we assume  $\Omega_m = 0.3$ ,  $\Omega_\Lambda = 0.7$ , and  $h = 0.7$ . All magnitudes given are on the AB system.

## 2. Data

### 2.1. Hyper Suprime-Cam Imaging Data

The HSC SSP (Aihara et al. 2018b) is an ongoing imaging survey with the Hyper Suprime-Cam (HSC; Miyazaki et al. 2012, 2018; Furusawa et al. 2018; Kawanomoto et al. 2018; Komiyama et al. 2018) on the Subaru Telescope. The Wide component of the HSC SSP will observe a  $\sim 1400 \text{ deg}^2$  area in the *grizy* bands to a depth of  $i = 26.2$ . The data used in this study are taken from Data Release 2 of the HSC SSP, which comprises data taken through the S17A semester and covers  $776 \text{ deg}^2$  in all bands, including  $289 \text{ deg}^2$  to the full depth. The median *i*-band seeing of the data is  $\sim 0.6''$ . The data are reduced with *hscPipe* version 5.4.0 (Bosch et al. 2018), which is based on the Large Synoptic Survey Telescope (LSST) pipeline (Axelrod et al. 2010; Jurić et al. 2017).

The photometric redshifts used in this analysis are determined using the MIZUKI algorithm (Tanaka 2015). A description of its application to the HSC SSP data is presented in Tanaka et al. (2018). The robustness of the photometric redshifts is a function of galaxy redshift and brightness, and is quantified in terms of  $\Delta z / (1 + z_{\text{ref}})$ , where  $\Delta z \equiv |z - z_{\text{ref}}|$  and  $z_{\text{ref}}$  is a reference redshift. The galaxies that we use to quantify the environment and LOS effects are brighter than  $i = 24$ . Roughly 97% of these galaxies have a photometric redshift of  $z \leq 2$ , which is approximately the median source redshift expected for lenses discovered in similar imaging surveys (Collett 2015). For HSC SSP galaxies that are brighter than  $i = 24$  and that are assigned a photometric redshift  $z_{\text{phot}} \leq 2$ , MIZUKI has a photometric redshift scatter of  $\sigma_{\text{conv}} = 0.047$  and a catastrophic outlier rate (defined as the fraction of objects such that  $\Delta z / (1 + z_{\text{true}}) > 0.15$ ) of 9.0%.

### 2.2. BOSS Spectroscopic Data

Our sample of strong lenses using various search algorithms (Section 4.1) is based on a pre-selection of candidate lens galaxies. These candidates are taken from the Baryon Oscillation Spectroscopic Survey (BOSS; Dawson et al. 2013), a component of the Sloan Digital Sky Survey III (SDSS-III; Eisenstein et al. 2011). The BOSS sample consists of the LOWZ subsample (primarily  $z < 0.4$  LRGs) and the CMASS subsample (primarily  $0.4 < z < 0.7$  LRGs). The initial sample of SuGOHI-g lenses used the BOSS Data Release 12 (Alam et al. 2015). The lens galaxy velocity dispersions used in this study come from Data Release 14 (Abolfathi et al. 2018).

## 3. New Lens Candidates in Data Release 2 of the HSC SSP

The SuGOHI-g sample of lenses are found through a combination of several lens search methodologies, which are described in Sonnenfeld et al. (2018). The primary search method is the YATTALENS algorithm, which searches for arc-like features around massive galaxies and fits simple lens models to evaluate the likelihood of those systems being lenses.

The new lens candidates discovered in Data Release 2 of the HSC SSP and presented here are found with YATTALENS.

We run YATTALENS on 31,286 massive galaxies in BOSS and find 772 lens candidates, 131 of which are in the LOWZ subsample and 641 of which are in the CMASS subsample. These candidates are visually inspected by the coauthors and individually graded using the following scheme:

1. Grade A: definite lenses.
2. Grade B: probable lenses.
3. Grade C: possible lenses.
4. Grade D: nonlenses.

In total, we find 7 new lenses with an average grade of A, 34 with an average grade of B, and 159 with an average grade of C. The full list of candidates, including grade C systems, can be found online.<sup>16</sup> We present newly discovered lenses with an average grade of A or B in Table 1. We show images of the grade A lenses in Figure 1 and the grade B lens candidates in Figure 2. The BOSS spectra are visually inspected to identify emission lines from the lensed source, and thus measure the source redshift. However, we are only able to measure the source redshift for one system in the new sample of grade A or B lenses.

## 4. Sample Selection for Environment and LOS Analysis

### 4.1. Lens Sample

The sample of lenses used in this study includes the previously discovered candidates from Sonnenfeld et al. (2018) along with new candidates discovered in Data Release 2 (Section 3). We only use lenses whose average grades are A or B (definite or probable lenses). To increase our sample size of lenses, we also include previously known lenses in our sample. We search the Master Lens Database<sup>17</sup> (L. A. Moustakas et al. 2019, in preparation), selecting for systems with a grade of A or B where the lensing object is a galaxy (as opposed to a galaxy group or cluster). The Master Lens Database uses a grading scheme qualitatively similar to our own, and many of the lenses have follow-up *HST* imaging and/or spectroscopically confirmed source redshifts, so we expect these to be real lenses with high confidence. We add two additional known lenses in the survey area, HSCJ142449–005321 (the “Eye of Horus”; Tanaka et al. 2016) and H-ATLAS J090740.0–004200 (“SDP.9”; Negrello et al. 2010). We further include two new grade A and B galaxy-scale lenses that have subsequently been discovered by the CHITAH algorithm (Chan et al. 2015). These were originally classified as grade C lenses by Sonnenfeld et al. (2018), but were given higher grades by the classifiers in J. H. H. Chan et al. (2019, in preparation).

We manually remove systems where there is clearly more than one galaxy contributing to the strong lensing (i.e., there are multiple galaxies within the region enclosed by the lensed images). Some lenses outside of the SuGOHI-g sample do not have velocity dispersion measurements from BOSS, while others have measured velocity dispersions smaller than 100 km s<sup>-1</sup> or larger than 400 km s<sup>-1</sup>, indicative of significant errors in their measurement. We do not include these lenses in our analysis since we cannot build a sample of twin galaxies for them, but we can still calculate their local and LOS environments. Our final

lens sample, which we refer to as the “main sample,” contains 87 lenses with a mean lens redshift of  $\langle z_L \rangle = 0.514$  and is presented in Table 2. For completeness, we show the results for individual lenses not in the main sample in Appendix A.

### 4.2. Twin Sample

We construct a sample of “twin” galaxies for comparison with the lens sample in a manner similar to that of Treu et al. (2009). We select galaxies from the BOSS DR14 using the same selection criteria as for the pre-selected galaxies used as targets for the YATTALENS algorithm, excluding the galaxies in the lens sample itself. We then construct the twin sample based on galaxy redshift and velocity dispersion.

The strong lensing cross section of a galaxy is a steep function of its velocity dispersion ( $\propto \sigma^4$  for an isothermal mass profile). Given this fact, a lensing-selected sample effectively selects galaxies based on their true velocity dispersion, which could result in an Eddington bias due to which the measured velocity dispersions of our lens sample from BOSS are systematically low. This would result in our selection of the twin sample to select less massive galaxies than the lenses if we did a simple matching based on measured velocity dispersion. The expected velocity dispersion of a galaxy (assuming a singular isothermal sphere profile) is

$$\sigma_{\text{SIS}} = c \sqrt{\frac{\theta_E}{4\pi} \frac{D_S}{D_{\text{LS}}}}. \quad (1)$$

We can then compare the expected velocity dispersion to the lenses’ measured velocity dispersions from BOSS. We have a subsample of 10 lens systems in which we have measured source redshifts and Einstein radii from the literature, and therefore can compare their expected  $\sigma_{\text{SIS}}$  to their measured velocity dispersion from BOSS. Of these 10 systems, 9 have a  $\sigma_{\text{SIS}}$  larger than their measured  $\sigma$  with a mean difference between the two quantities of  $\sim 15\%$ . While this subsample is small, it suggests that this bias is real. For the SLACS sample, Bolton et al. (2008) find that  $\sigma/\sigma_{\text{SIS}} \approx 0.948$  before correcting for differences in the physical sizes of the SDSS fiber aperture at the lens redshift. This likely has a smaller influence in our sample due to our higher mean lens redshift, and the magnitude of the effect does not seem large enough to explain this bias. Therefore, we must account for this effect when selecting the twin sample.

For each lens galaxy, we assume the probability distribution of its velocity dispersion is a Gaussian with a mean and scatter given by the value and uncertainty from BOSS. We then weight this distribution by  $\sigma^4$  and renormalize, taking the mean of the new distribution to be the “corrected” velocity dispersion. On average, the corrected lens galaxy velocity dispersions are  $\sim 13\%$  higher than the measured values. For each lens, we then randomly pick 10 twin galaxies that have a spectroscopic redshift such that  $\Delta z/(1 + z_L) \leq 0.01$  and a velocity dispersion that is within 10% of the lens galaxy’s corrected velocity dispersion. We also enforce a condition that half of the twins have a smaller velocity dispersion and half have a larger velocity dispersion than that of their corresponding lens to minimize bias from the slope of the galaxy velocity dispersion function. The same galaxy can be selected more than once if it is a “twin” of more than one lens galaxy.

<sup>16</sup> <http://hsc.mtk.nao.ac.jp/ssp/science/strong-lensing>

<sup>17</sup> <http://masterlens.astro.utah.edu/>

**Table 1**  
Grade A Lenses and Grade B Candidates in Data Release 2 of the HSC SSP

Name	$\alpha$ (J2000)	$\delta$ (J2000)	$z_L$	$z_S$	Subsample	Grade
HSCJ015618–010747	29.0755	−1.1298	0.542	1.170	CMASS	B
HSCJ015750–003818	29.4599	−0.6385	0.520	...	CMASS	B
HSCJ093506–020031	143.7761	−2.0089	0.531	...	CMASS	B
HSCJ094123+000446	145.3460	0.0796	0.486	...	CMASS	B
HSCJ095750+014507	149.4587	1.7521	0.574	...	CMASS	B
HSCJ100659+024735	151.7470	2.7931	0.482	...	CMASS	B
HSCJ114311–013935	175.7970	−1.6598	0.644	...	CMASS	B
HSCJ122048+002145	185.2014	0.3628	0.407	...	LOWZ	B
HSCJ122314–002939	185.8114	−0.4944	0.547	...	CMASS	B
HSCJ123825+003212	189.6043	0.5368	0.478	...	CMASS	B
HSCJ124320–004517	190.8365	−0.7550	0.654	...	CMASS	A
HSCJ125251+005805	193.2132	0.9683	0.540	...	CMASS	B
HSCJ125254+004356	193.2275	0.7323	0.649	...	CMASS	A
HSCJ134351+010817	205.9665	1.1382	0.567	...	CMASS	B
HSCJ135038+002550	207.6591	0.4306	0.526	...	CMASS	B
HSCJ135138+002839	207.9122	0.4778	0.461	...	CMASS	A
HSCJ135242–002614	208.1791	−0.4372	0.508	...	CMASS	B
HSCJ135853–021525	209.7230	−2.2571	0.737	...	CMASS	B
HSCJ141001+012956	212.5044	1.4992	0.541	...	CMASS	B
HSCJ142241+424608	215.6716	42.7689	0.605	...	CMASS	B
HSCJ142353+013446	215.9711	1.5797	0.519	...	CMASS	B
HSCJ145242+425731	223.1789	42.9589	0.718	...	CMASS	A
HSCJ145759+423019	224.4966	42.5053	0.607	...	CMASS	B
HSCJ151336+433251	228.4032	43.5475	0.487	...	CMASS	B
HSCJ220550+041524	331.4591	4.2569	0.268	...	LOWZ	B
HSCJ221234+045456	333.1438	4.9158	0.262	...	LOWZ	B
HSCJ221315+034536	333.3137	3.7602	0.446	...	LOWZ	B
HSCJ224454+031551	341.2286	3.2642	0.791	...	CMASS	B
HSCJ224800–010259	342.0030	−1.0499	0.277	...	LOWZ	B
HSCJ225800+004533	344.5026	0.7594	0.576	...	CMASS	B
HSCJ230521–000211	346.3403	−0.0366	0.492	...	CMASS	A
HSCJ230658+022543	346.7428	2.4286	0.362	...	LOWZ	B
HSCJ231004+024759	347.5196	2.7999	0.390	...	LOWZ	B
HSCJ231145–013039	347.9379	−1.5109	0.400	...	LOWZ	B
HSCJ231555+012906	348.9800	1.4850	0.424	...	LOWZ	B
HSCJ232415+011331	351.0652	1.2255	0.592	...	CMASS	B
HSCJ233130+003733	352.8770	0.6259	0.552	...	CMASS	A
HSCJ233146+013845	352.9434	1.6460	0.476	...	CMASS	A
HSCJ233230+003821	353.1289	0.6394	0.623	...	CMASS	B
HSCJ233311+022310	353.2963	2.3864	0.472	...	CMASS	B
HSCJ233528+001355	353.8677	0.2322	0.568	...	CMASS	B

**Note.** New lens candidates in Data Release 2 of the HSC SSP. Columns 4 and 5 list the lens and source redshift (when measured), respectively. Column 6 lists which subsample of BOSS LRGs the lens galaxy belongs to. Column 7 indicates the grade of the candidate.

Our final twin sample contains 870 galaxies, of which 855 are unique.

#### 4.3. Control Fields

We select random control fields from the HSC SSP by randomly selecting patches ( $12' \times 12'$  square regions) from the survey patch catalog and then selecting random coordinates within that patch. The chosen locations are taken to be the center of each control field. Patches that have `imag_psf_depth < 24` are excluded in order to remove fields that do not have a similar depth to the lens fields. We also exclude patches that do not have a defined PSF magnitude depth in the other four filters, indicating that they lack coverage in all five bands. The control sample consists of 100 random fields that meet these criteria, which is a large enough sample to obtain good statistics within a reasonable computation time. In principle, the randomly chosen control fields can overlap with each other or

with the lens and twin fields, but we verify that none of the fields overlap to within a  $120''$  radius.

#### 4.4. Correction for Survey Gaps

The HSC SSP area has gaps due to survey edges, chip gaps, bright star masks, etc. To account for this, we use the HSC SSP random point catalog (Coupon et al. 2018), which contains randomly sampled points in the survey region that are flagged in the same way as the objects. The random points are drawn with a density of 100 points per  $\text{arcmin}^2$ . When evaluating galaxy number counts within our selected apertures, we use the random point catalog to correct the raw counts,  $N$ , by a scaling factor to account for occulted area in the aperture. We define the effective number counts as

$$N_{\text{eff}} \equiv N \times \frac{100\pi r_{\text{ap}}^2}{N_{\text{rand}}}, \quad (2)$$

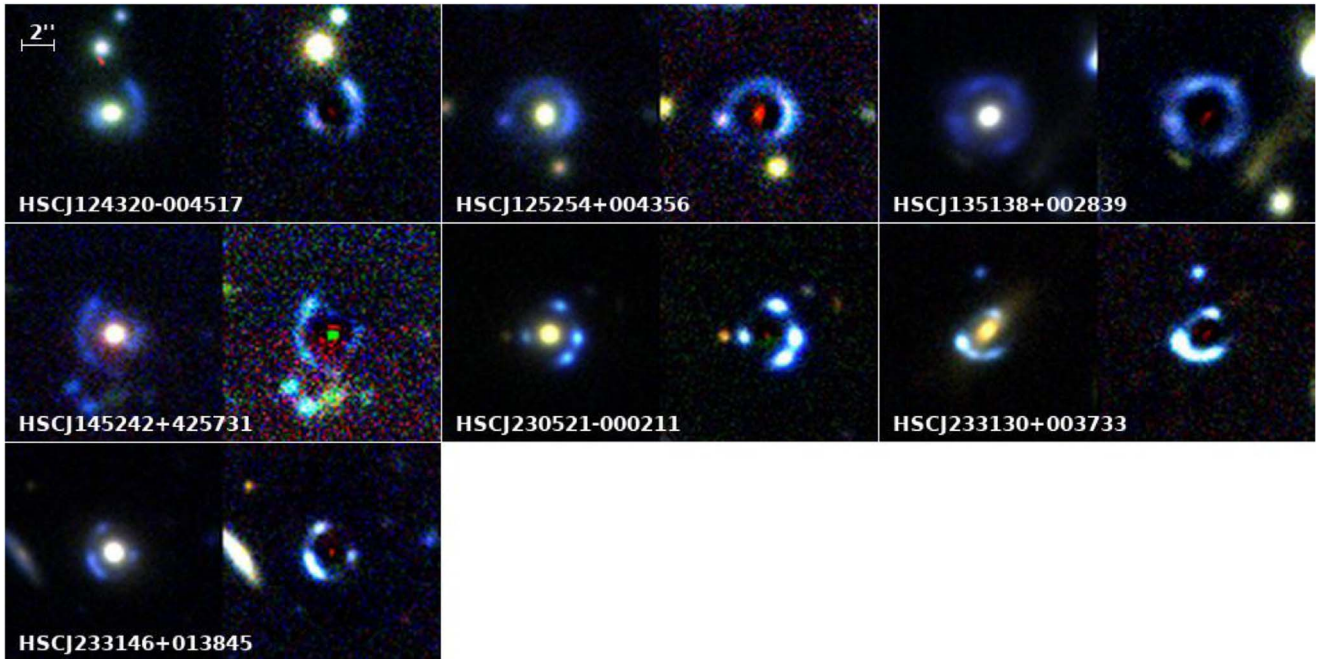


**Figure 1.** Grade A lenses. For each system, the left-hand panel is a color-composite image in  $g$ ,  $r$ , and  $i$  bands, while the right-hand panel is a lens-subtracted version of the image. A higher contrast is used in the right-hand panel to enhance the images of the lensed source.

where  $r_{\text{ap}}$  is the radius of the chosen aperture and  $N_{\text{rand}}$  is the number of points from the random catalog in the aperture. For small apertures and/or bright magnitude limits where the galaxy density is more sparse, this correction can lead to a bias toward higher  $N_{\text{eff}}$  in individual fields if most of them do not contain galaxies in the survey gaps (Cooper et al. 2005), but the ensemble of results over the entire sample should be unbiased.

If  $N_{\text{rand}}/(100\pi r_{\text{ap}}^2) < 0.75$ , we exclude that field from the calculation for that particular aperture and lens redshift. Rusu et al. (2017) similarly excluded fields from their analysis of the field of the time-delay lens HE 0435–1223, testing a cut of both 0.5 and 0.75, and finding that the results were insensitive to the choice of masked fraction threshold.

## 5. Quantifying LOS and Local Environment Overdensity

### 5.1. Galaxy Selection

To evaluate local and LOS densities, we select galaxies from the HSC SSP catalog that satisfy the following criteria, which are defined in Bosch et al. (2018):

1.  $i_{\text{extendedness\_value}} > 0$ .
2.  $i_{\text{cmodel\_mag}} \leq 24.0$ .
3.  $\text{merge\_peak\_i} = \text{True}$ .
4.  $\text{isprimary} = \text{True}$ .
5.  $i_{\text{cmodel\_flag}} = \text{False}$ .
6.  $i_{\text{pixelflags\_edge}} = \text{False}$ .
7.  $i_{\text{pixelflags\_bad}} = \text{False}$ .
8.  $i_{\text{pixelflags\_saturatedcenter}} = \text{False}$ .
9.  $i_{\text{pixelflags\_crcenter}} = \text{False}$ .

We further require that galaxies lie in patches that have observations in all five bands, even if not to the full survey depth, as the photometric redshifts are less reliable without measurements in all filters. The galaxy magnitudes used in this analysis are cModel magnitudes, which are measured by fitting

galaxy models convolved with the point-spread function (PSF) to the light profile of the object (Abazajian et al. 2004). The photometric redshift and  $i$ -band magnitude distributions of galaxies selected by these criteria within  $r \leq 120''$  of all control fields are shown in Figure 3.

For our calculation of  $N_{\text{eff}}$ , we select points from the random point catalog using the following criteria:

1.  $\text{isprimary} = \text{True}$ .
2.  $i_{\text{pixelflags\_edge}} = \text{False}$ .
3.  $i_{\text{pixelflags\_bad}} = \text{False}$ .
4.  $i_{\text{pixelflags\_saturatedcenter}} = \text{False}$ .
5.  $i_{\text{pixelflags\_crcenter}} = \text{False}$ .

### 5.2. Line of Sight Structure

We quantify the density of a LOS by the effective galaxy number counts,  $N_{\text{eff}}$ , brighter than a limiting  $i$ -band magnitude and within a projected radial distance  $r_{\text{ap}}$  of each lens. We exclude galaxies that are within  $2''.5$  of the lens and twin samples to remove any background galaxies strongly affected by magnification bias (e.g., Fassnacht et al. 2011), and exclude a similar region from the centers of the control fields so that we are comparing similar volumes. We test aperture sizes of  $r_{\text{ap}} = \{30'', 60'', 90'', 120''\}$  and limiting magnitudes of  $i \leq \{21.0, 22.0, 23.0, 24.0\}$ . Collett et al. (2013) suggest that galaxies projected further than  $120''$  from a lens galaxy and fainter than  $i = 24$  are unlikely to make a significant contribution to the external convergence. These limits also encompass the aperture sizes and limiting magnitudes tested by Rusu et al. (2017) in evaluating the external convergence in HE 0435–1223.

To separate the contribution of the local lens environment from the LOS, we remove galaxies that are close to the lens in redshift. We define  $N_{\text{eff}}^{\text{LOS}}$  to be  $N_{\text{eff}}$  calculated without counting the galaxies that have photometric redshifts such that

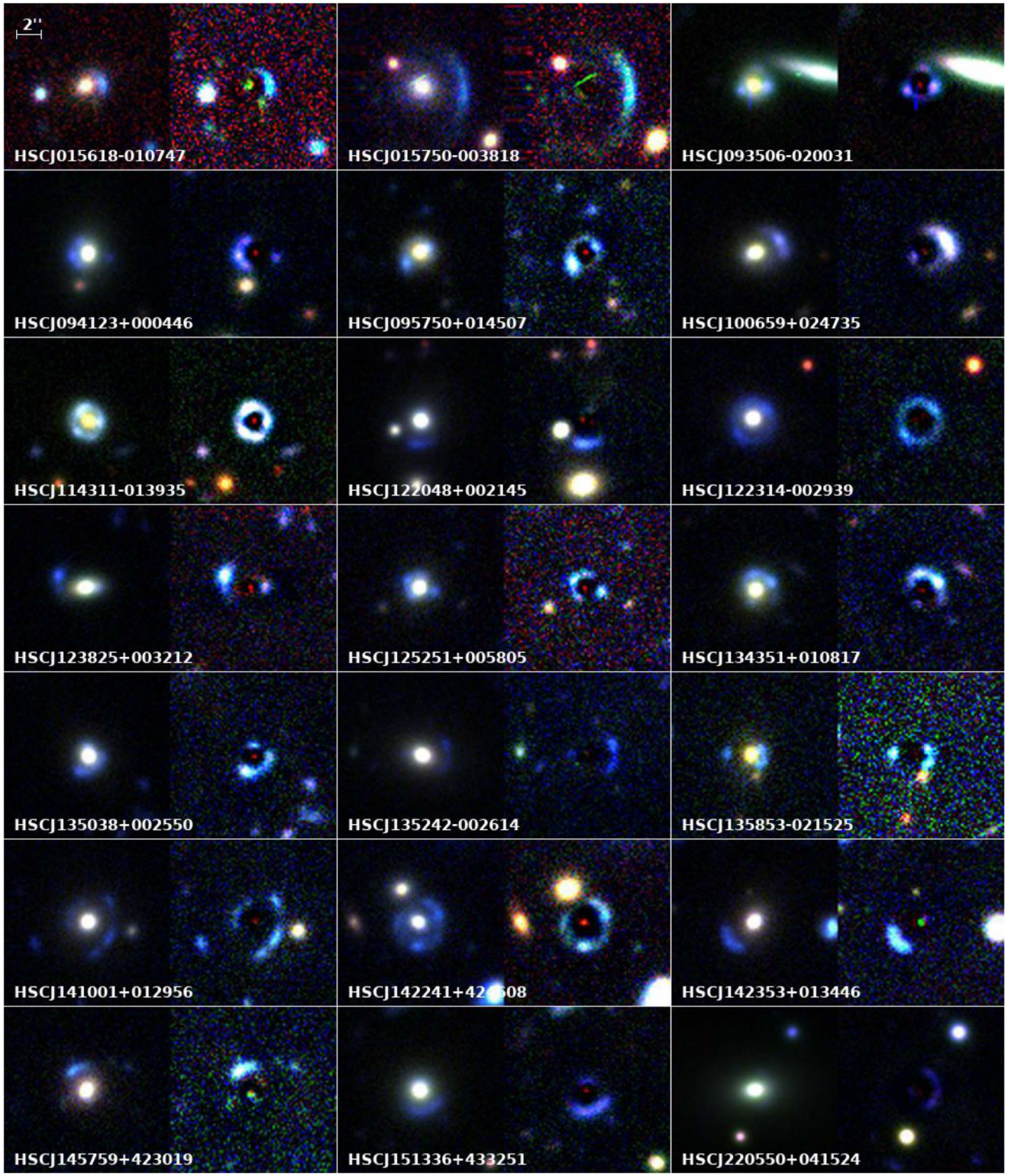


**Figure 2.** Grade B lens candidates. For each system, the left-hand panel is a color-composite image in  $g$ ,  $r$ , and  $i$  bands, while the right-hand panel is a lens-subtracted version of the image. A higher contrast is used in the right-hand panel to enhance the images of the lensed source.

$\Delta z/(1 + z_L) \leq 0.05$ . The threshold of 0.05 is taken to be a conservative estimate of the typical scatter of the MIZUKI photometric redshift algorithm out to  $i = 24$  when applied to HSC SSP data (Tanaka et al. 2018).

We can calculate the fractional overdensity of a lens LOS relative to a random LOS by normalizing  $N_{\text{eff}}$  by a factor of

$\langle N_{\text{eff}}^{\text{cont}} \rangle$ , which is the mean  $N_{\text{eff}}$  across all control fields for the same aperture size and limiting magnitude. To ensure that we are comparing equivalent volumes, we exclude a redshift slice of width  $\Delta z/(1 + z_{L,\text{rand}}) \leq 0.05$  centered on a randomly drawn lens redshift for each control field when calculating  $\langle N_{\text{eff}}^{\text{cont}} \rangle$ . The uncertainties are taken to be the combination of

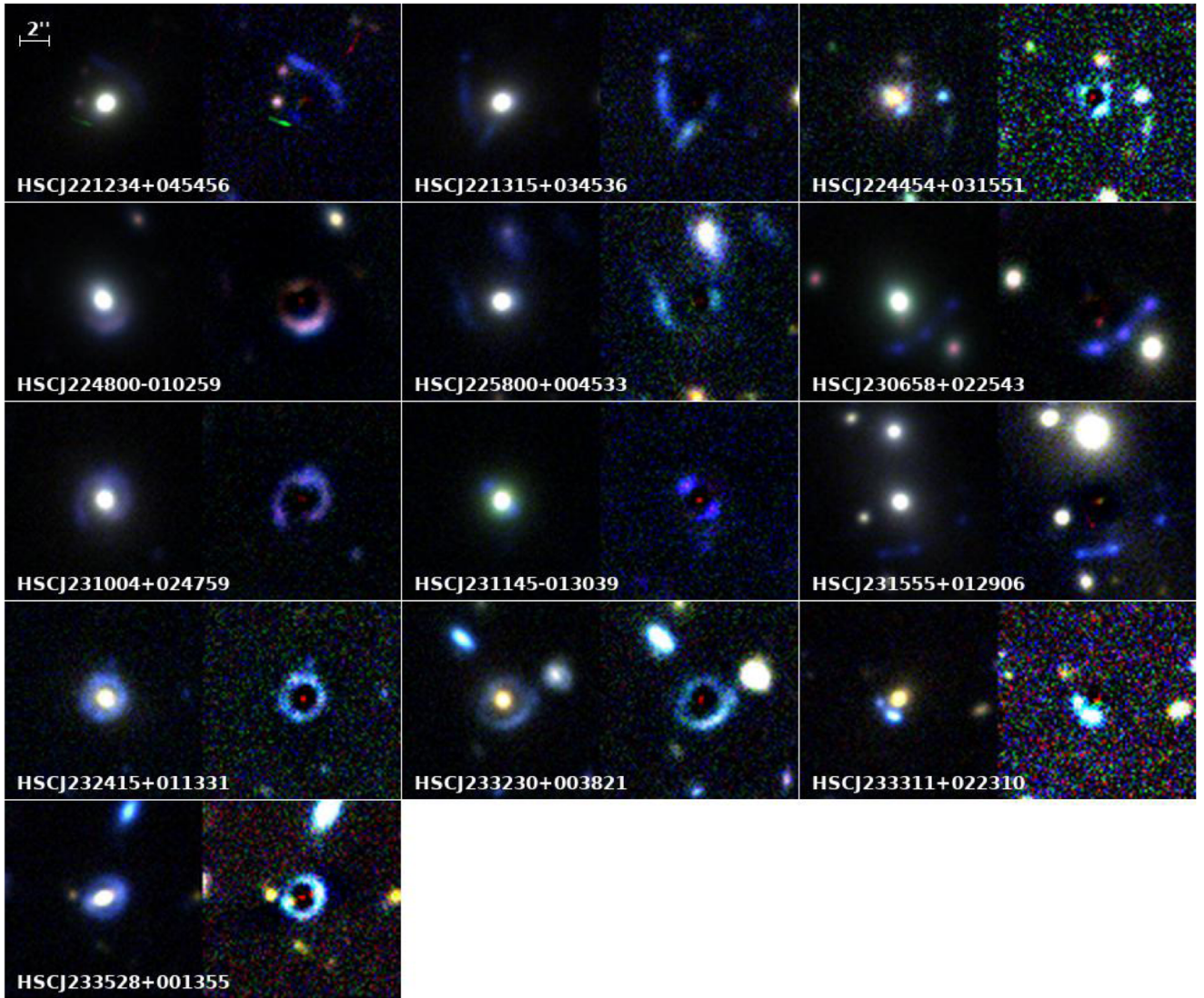


Figure 2. (Continued.)

Poisson error on  $N$  and  $N_{\text{rand}}$  in the calculation of  $N_{\text{eff}}$ , along with the error on the mean of  $N_{\text{eff}}^{\text{cont}}$ . This is a conservative estimate, as Poisson error on  $N$  dominates the uncertainty budget. For certain applications, it may be useful to have the uncertainties that do not include Poisson error on  $N$  (e.g., Rusu et al. 2017), so we show these values in Appendix B. We ignore Poisson uncertainties in the  $N_{\text{eff}}$  calculations for individual control fields, as they are negligible in comparison to the sample variance.

### 5.3. Local Lens Environment

To evaluate the local overdensity in the environment of a lens or twin galaxy, we use a standard measure of environment,  $\Sigma_{10}$  (e.g., Dressler 1980; Cooper et al. 2006; Treu et al. 2009), defined as

$$\Sigma_{10} = \frac{10}{\pi D_{p,10}^2}, \quad (3)$$

where  $D_{p,10}$  is the projected distance in megaparsecs to the tenth nearest neighbor that is brighter than  $i = 24$  and has a redshift within  $\Delta z/(1 + z_L) \leq 0.05$  of the lens redshift. Cooper et al. (2005)

find that  $D_{p,10}$  is a reasonable estimator of local galaxy environments over a broad range of scales and is reasonably robust to survey edge effects. We correct the  $\Sigma_{10}$  values for the survey geometry using the random object catalog to calculate a scaling factor as in Equation (2), using  $r_{\text{ap}} = D_{p,10}$ .

The absolute  $\Sigma_{10}$  values depend on the chosen magnitude cut and lens redshift. Therefore in practice, we use a normalized density,  $\Sigma_{10}/\langle \Sigma_{10}^{\text{cont}} \rangle$ , where  $\langle \Sigma_{10}^{\text{cont}} \rangle$  is the mean  $\Sigma_{10}$  evaluated at the center of each of the control fields at the same redshift as the lens being considered. We take the uncertainty on this relative density measure to be the combination of Poisson error on  $n = 10$  in the calculation of  $\Sigma_{10}$  and the error on the mean of  $\Sigma_{10}^{\text{cont}}$ , similar to Treu et al. (2009).

## 6. Results and Discussion

### 6.1. Lens Lines of Sight

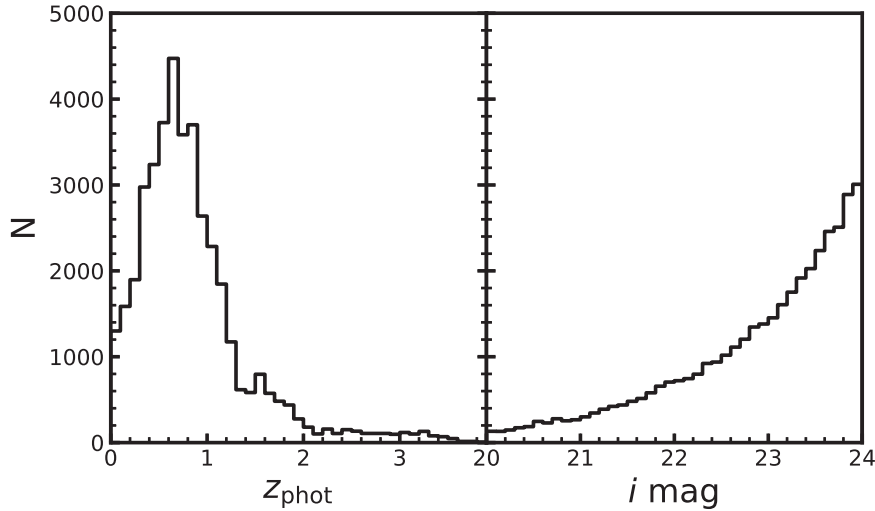
We show normalized histograms of  $N_{\text{eff}}$  for the lens, twin, and control LOSs in Figure 4. Each panel represents a different aperture size and magnitude cut. In general, the lens and twin LOSs have higher  $N_{\text{eff}}$  than the control sample. We quantify the significance of these differences using a two-sample Anderson–

**Table 2**  
Main Lens Sample

Lens	$\alpha$ (J2000)	$\delta$ (J2000)	$z_L$	$z_S$	$\sigma^a$ (km s $^{-1}$ )	Reference <sup>b</sup>
HSCJ015731–033057	29.3812	−3.5160	0.621	...	190 ± 56	SuGOHI I
HSCJ015756–021809	29.4859	−2.3028	0.372	...	244 ± 17	SuGOHI I
SDSSJ0157–0056	29.4956	−0.9406	0.513	0.924	238 ± 35	Bolton et al. (2008)
HSCJ020141–030946	30.4249	−3.1628	0.362	...	272 ± 32	SuGOHI I
HSCJ020241–064611	30.6725	−6.7698	0.502	2.75	155 ± 27	SuGOHI I
HSCJ020846–032727	32.1952	−3.4577	0.618	...	140 ± 39	SuGOHI I
SL2SJ021737–051329	34.4048	−5.2248	0.644	1.847	305 ± 60	Sonnenfeld et al. (2013a)
HSCJ022140–021020	35.4172	−2.1723	0.708	...	289 ± 140	SuGOHI I
SL2SJ022315–062906	35.8142	−6.4851	0.550	...	305 ± 43	More et al. (2012)
SL2SJ022346–053418	35.9423	−5.5718	0.499	1.44	258 ± 27	Sonnenfeld et al. (2013a)
SL2SJ022357–065142	35.9914	−6.8618	0.473	...	116 ± 35	Sonnenfeld et al. (2013a)
SL2SJ022439–040045	36.1628	−4.0125	0.430	...	191 ± 36	More et al. (2012)
SL2SJ022511–045433	36.2960	−4.9093	0.238	1.199	249 ± 13	Sonnenfeld et al. (2013a)
SL2SJ022610–042011	36.5444	−4.3366	0.494	1.232	233 ± 39	Sonnenfeld et al. (2013a)
HSCJ023217–021703	38.0724	−2.2844	0.508	...	263 ± 127	SuGOHI I
SL2SJ023307–043838	38.2795	−4.6439	0.671	1.87	325 ± 123	More et al. (2012)
HSCJ023538–063406	38.9093	−6.5684	0.181	...	241 ± 11	SuGOHI I
HSCJ023637–033220	39.1554	−3.5389	0.270	...	263 ± 19	SuGOHI I
HSCJ023655–023656	39.2303	−2.6156	0.562	...	184 ± 41	SuGOHI I
HSCJ083943+004740	129.9293	0.7947	0.621	...	302 ± 37	SuGOHI I
HSCJ085855–010208	134.7333	−1.0357	0.468	1.42	167 ± 27	SuGOHI I
HSCJ090507–001030	136.2806	−0.1750	0.494	...	162 ± 24	SuGOHI I
HSCJ090709+005648	136.7904	0.9468	0.478	...	246 ± 37	SuGOHI I
SDSSJ0915–0055	138.8192	−0.9168	0.402	1.1705	210 ± 15	Brownstein et al. (2012)
HSCJ091608+034710	139.0355	3.7862	0.531	...	299 ± 33	J. H. H. Chan et al. (2019, in preparation)
HSCJ091904+033638	139.7692	3.6107	0.444	...	248 ± 25	SuGOHI I
HSCJ092101+035521	140.2565	3.9228	0.472	...	175 ± 26	J. H. H. Chan et al. (2019, in preparation)
HSCJ093506–020031	143.7761	−2.0089	0.531	...	235 ± 38	SuGOHI II
HSCJ094123+000446	145.3460	0.0796	0.486	...	255 ± 29	SuGOHI II
SDSSJ0944–0147	146.1145	−1.7951	0.539	1.179	199 ± 38	Brownstein et al. (2012)
HSCJ095750+014507	149.4587	1.7521	0.574	...	161 ± 36	SuGOHI II
COSMOS0013+2249	150.0579	2.3803	0.346	...	234 ± 40	Faure et al. (2011)
COSMOS0056+1226	150.2366	2.2072	0.361	0.808	241 ± 29	Faure et al. (2011)
HSCJ100659+024735	151.7470	2.7931	0.482	...	246 ± 40	SuGOHI II
HSCJ114311–013935	175.7970	−1.6598	0.644	...	226 ± 38	SuGOHI II
HSCJ115653–003948	179.2210	−0.6635	0.508	...	187 ± 39	SuGOHI I
HSCJ120623+001507	181.5994	0.2520	0.563	3.12	266 ± 48	SuGOHI I
HSCJ121052–011905	182.7187	−1.3181	0.700	...	285 ± 71	SuGOHI I
HSCJ122048+002145	185.2014	0.3628	0.407	...	285 ± 24	SuGOHI II
HSCJ122314–002939	185.8114	−0.4944	0.547	...	276 ± 34	SuGOHI II
HSCJ123825+003212	189.6043	0.5368	0.478	...	259 ± 45	SuGOHI II
HSCJ124320–004517	190.8365	−0.7550	0.654	...	365 ± 65	SuGOHI II
HSCJ125254+004356	193.2275	0.7323	0.649	...	388 ± 59	SuGOHI II
HSCJ134351+010817	205.9665	1.1382	0.567	...	260 ± 63	SuGOHI II
HSCJ135038+002550	207.6591	0.4306	0.526	...	210 ± 47	SuGOHI II
HSCJ135138+002839	207.9122	0.4778	0.461	...	355 ± 56	SuGOHI II
HSCJ135242–002614	208.1791	−0.4372	0.508	...	364 ± 45	SuGOHI II
HSCJ135853–021525	209.7230	−2.2571	0.737	...	225 ± 44	SuGOHI II
HSCJ140929–011410	212.3738	−1.2363	0.584	...	204 ± 39	SuGOHI I
HSCJ141001+012956	212.5044	1.4992	0.541	...	257 ± 34	SuGOHI II
HSCJ141300–012608	213.2503	−1.4356	0.749	...	248 ± 65	SuGOHI I
HSCJ141831–000052	214.6309	−0.0146	0.263	...	260 ± 13	SuGOHI I
HSCJ142353+013446	215.9711	1.5797	0.519	...	374 ± 43	SuGOHI II
HSCJ142449–005321	216.2042	−0.8893	0.795	$z_{S1} = 1.302; z_{S2} = 1.988$	246 ± 94	Tanaka et al. (2016)
HSCJ142720+001916	216.8356	0.3211	0.551	...	250 ± 32	SuGOHI I
HSCJ142748+000958	216.9515	0.1663	0.589	...	281 ± 72	SuGOHI I
HSCJ144307–004056	220.7798	−0.6823	0.500	1.07	251 ± 35	SuGOHI I
HSCJ144428–005142	221.1198	−0.8618	0.575	...	199 ± 27	SuGOHI I
HSCJ145236–002142	223.1527	−0.3617	0.733	...	325 ± 47	SuGOHI I
HSCJ145732–015917	224.3858	−1.9882	0.526	...	238 ± 40	SuGOHI I
HSCJ145759+423019	224.4966	42.5053	0.607	...	272 ± 68	SuGOHI II
HSCJ145902–012351	224.7613	−1.3975	0.482	...	268 ± 40	SuGOHI I
HSCJ151336+433251	228.4032	43.5475	0.487	...	204 ± 26	SuGOHI II
HSCJ155826+432830	239.6111	43.4752	0.444	...	292 ± 30	SuGOHI I

**Table 2**  
(Continued)

Lens	$\alpha$ (J2000)	$\delta$ (J2000)	$z_L$	$z_S$	$\sigma^a$ (km s $^{-1}$ )	Reference <sup>b</sup>
SL2SJ220202+014710	330.5069	1.7860	0.300	...	213 ± 8	More et al. (2012)
SL2SJ220506+014703	331.2788	1.7844	0.476	2.53	269 ± 46	Sonnenfeld et al. (2013a)
HSCJ220550+041524	331.4591	4.2569	0.268	...	221 ± 15	SuGOHI II
SL2SJ220642+041131	331.6751	4.1919	0.620	...	226 ± 38	More et al. (2012)
HSCJ221726+000350	334.3602	0.0640	0.398	...	216 ± 20	SuGOHI I
SL2SJ221852+014038	334.7193	1.6775	0.564	...	264 ± 44	Sonnenfeld et al. (2013a)
HSCJ222801+012805	337.0082	1.4683	0.647	...	336 ± 49	SuGOHI I
HSCJ223518–004747	338.8263	−0.7965	0.640	...	196 ± 54	SuGOHI I
HSCJ223733+005015	339.3897	0.8377	0.604	...	256 ± 42	SuGOHI I
HSCJ224201+022810	340.5049	2.4696	0.443	...	189 ± 49	SuGOHI I
HSCJ224221+001144	340.5899	0.1958	0.385	...	256 ± 20	SuGOHI I
HSCJ224454+031551	341.2286	3.2642	0.791	...	277 ± 68	SuGOHI II
HSCJ224800–010259	342.0030	−1.0499	0.277	...	245 ± 13	SuGOHI II
HSCJ225800+004533	344.5026	0.7594	0.576	...	280 ± 45	SuGOHI II
SDSSJ2303+0037	345.8965	0.6176	0.458	0.936	269 ± 35	Brownstein et al. (2012)
HSCJ230521–000211	346.3403	−0.0366	0.492	...	185 ± 28	SuGOHI II
HSCJ231004+024759	347.5196	2.7999	0.390	...	270 ± 28	SuGOHI II
HSCJ231145–013039	347.9379	−1.5109	0.400	...	241 ± 31	SuGOHI II
HSCJ232415+011331	351.0652	1.2255	0.592	...	296 ± 63	SuGOHI II
HSCJ233130+003733	352.8770	0.6259	0.552	...	168 ± 41	SuGOHI II
HSCJ233146+013845	352.9434	1.6460	0.476	...	188 ± 62	SuGOHI II
HSCJ233311+022310	353.2963	2.3864	0.472	...	119 ± 47	SuGOHI II
HSCJ233528+001355	353.8677	0.2322	0.568	...	230 ± 43	SuGOHI II

**Notes.**<sup>a</sup> Velocity dispersions from SDSS DR14.<sup>b</sup> SuGOHI I = Sonnenfeld et al. (2018); SuGOHI II = this work.

**Figure 3.** Distribution of photometric redshift (left panel) and  $i$  magnitude (right panel) for galaxies satisfying our selection criteria within  $r \leq 120''$  of all control fields.

Darling test, from which we calculate  $P_{AD}$ , the significance level at which the null hypothesis that the two samples are drawn from the same parent distribution can be rejected (i.e., a lower  $P_{AD}$  means that it is less likely that the null hypothesis is true). Commonly accepted significance levels are  $P_{AD} < 0.05$  ( $2\sigma$ ) or  $P_{AD} < 0.003$  ( $3\sigma$ ). We perform this test in a pairwise manner among the lens, twin, and control samples for each of the aperture sizes and magnitude cuts. These results are shown in Table 3.

Our results show that the lens and twin samples are consistent with each other and any differences are of marginal significance, as would be expected if lenses are representative

of the underlying population of galaxies of similar masses and redshifts. Furthermore, the lens fields (as well as the twin fields) show a distinct difference in their  $N_{eff}$  distributions compared to the control fields, with the lens fields skewed toward higher-density LOSs. This is consistent with the results of Fassnacht et al. (2011). The overdensities of each lens's LOS relative to the control sample is given in Table 4.

We then exclude galaxies close to the lens and twin galaxies in redshift space to examine the LOS effects alone. As mentioned in Section 5.2, we randomly draw a lens redshift from our sample of lens galaxies and exclude objects within a redshift slice centered on that redshift. Using this method we

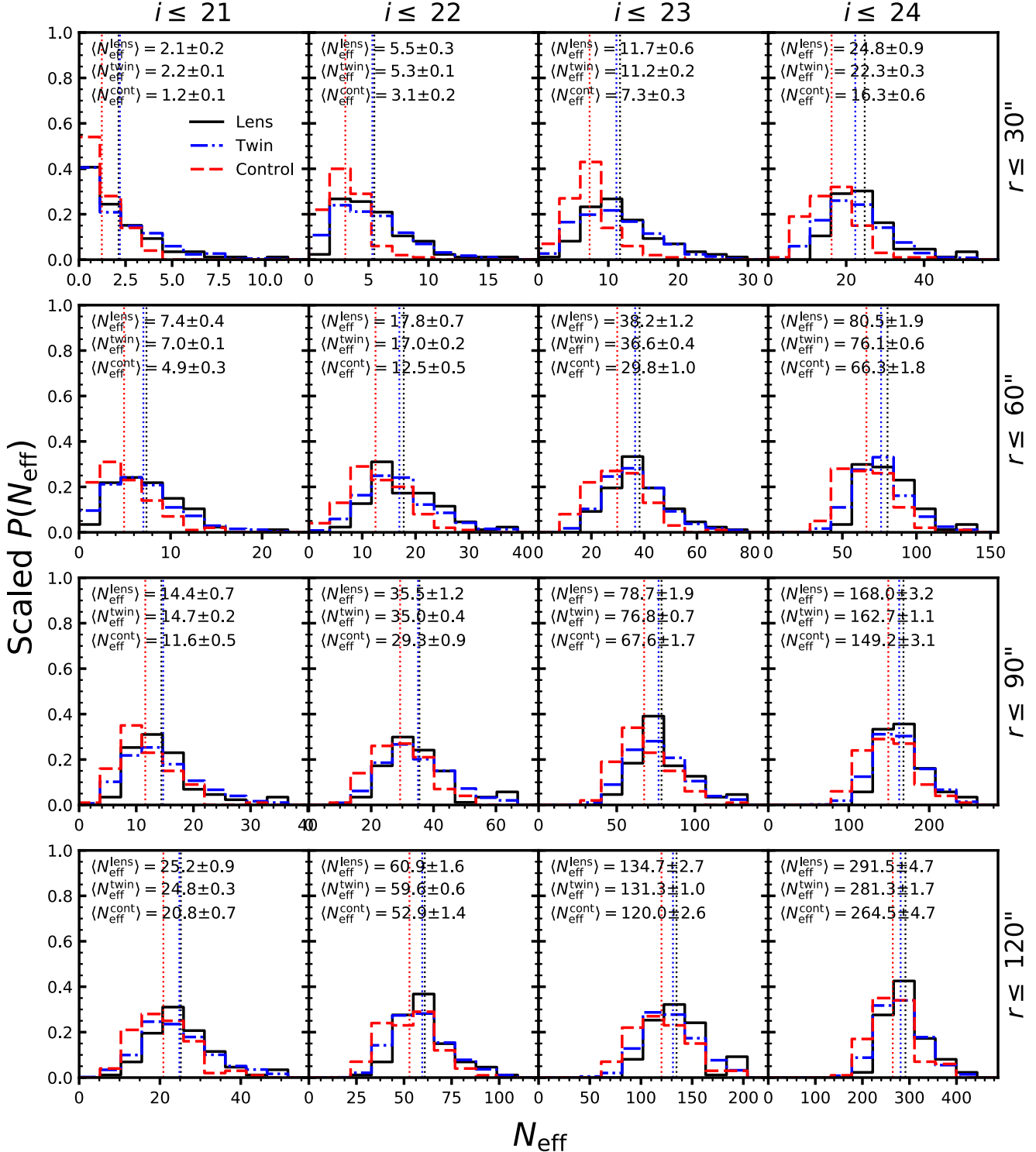


**Figure 4.** Scaled histogram of  $N_{\text{eff}}$  values for the lens (black solid line), twin (blue dotted-dashed line), and control (red dashed line) samples. The columns represent different limiting magnitudes, and the rows represent different aperture radii. The dotted lines of the corresponding color indicate the mean of the distributions. The mean and the standard error on the mean are given for the different samples within each panel. The lens and twin samples have higher  $N_{\text{eff}}$  in general than the control sample.

are comparing fair volumes across samples in our calculation. Figure 5 shows the  $N_{\text{eff}}$  histograms excluding those within our chosen redshift cuts. Table 5 shows the corresponding  $P_{\text{AD}}$  values.

Once the local environment of the lens galaxies are excluded, they are generally consistent with the control sample, particularly for larger aperture sizes where shot noise has a

smaller effect. This result affirms that of Fassnacht et al. (2011), showing that lenses do not lie along biased lines of sight. This is also consistent with the findings of Collett & Cunningham (2016) that show that lensed quasars have external convergence contributions of  $\kappa_{\text{ext}} < 0.01$  on average when considering just the projected LOS structure. There does appear to be a slight excess in the lens and twin samples, particularly at

**Table 3**  
Two-sample Anderson–Darling Test Significance Levels—Full LOS

Lens-control				
$r$ (arcsec)	$i \leq 21$	$i \leq 22$	$i \leq 23$	$i \leq 24$
30	<b>7.2e–04</b>	<b>8.1e–06</b>	<b>1.3e–05</b>	<b>1.7e–04</b>
60	<b>2.2e–05</b>	<b>8.8e–06</b>	<b>1.6e–05</b>	<b>1.1e–05</b>
90	<b>1.2e–03</b>	<b>1.7e–04</b>	<b>1.0e–04</b>	<b>1.0e–04</b>
120	<b>4.1e–04</b>	<b>4.5e–04</b>	<b>3.1e–04</b>	<b>1.7e–04</b>
Lens-twin				
$r$ (arcsec)	$i \leq 21$	$i \leq 22$	$i \leq 23$	$i \leq 24$
30	8.9e–01	6.2e–01	2.2e–01	2.0e–02
60	2.3e–01	2.7e–01	2.2e–01	5.9e–02
90	4.2e–01	4.9e–01	1.7e–01	1.6e–01
120	3.6e–01	2.4e–01	7.4e–02	3.5e–02
Twin-control				
$r$ (arcsec)	$i \leq 21$	$i \leq 22$	$i \leq 23$	$i \leq 24$
30	<b>1.7e–05</b>	<b>1.9e–04</b>	<b>3.0e–04</b>	<b>6.6e–04</b>
60	<b>1.3e–05</b>	<b>1.1e–05</b>	<b>8.9e–06</b>	<b>1.0e–05</b>
90	<b>3.7e–05</b>	<b>2.7e–05</b>	<b>7.0e–05</b>	<b>1.5e–04</b>
120	<b>1.7e–04</b>	<b>5.3e–04</b>	<b>7.4e–04</b>	<b>1.5e–03</b>

**Notes.** The values represent  $P_{AD}$ , the significance level at which the null hypothesis that the samples are drawn from the same parent distribution can be rejected. Values in italics are significant at greater than the  $2\sigma$  level, while values in bold are significant at greater than the  $3\sigma$  level.

small  $r_{ap}$  and/or bright limiting magnitudes where Poisson uncertainty due to small number statistics can be an issue. These excesses are not statistically significant in most of the individual panels of Figure 5 but appear consistently. We discuss a possible origin of this effect in Section 6.3.3.

## 6.2. Local Lens Environments

We compare the distribution of normalized  $\Sigma_{10}$  values of the lens and twin samples in Figure 6. The mean  $\Sigma_{10}/\langle\Sigma_{10}^{\text{cont}}\rangle$  for the lens and twin samples relative to the mean of the control fields are  $2.68 \pm 0.20$  and  $2.36 \pm 0.07$ , respectively. This shows that the local environments of both lenses and their twins are more overdense than those of randomly chosen galaxies, as expected. This also suggests a slight enhancement in the local density of lens galaxies compared to twins. A two-sample Anderson–Darling test of the two samples shows a  $P_{AD} = 0.005$ , which is marginally significant but cannot conclusively rule out lenses not exhibiting a particular bias in their local environment. Treu et al. (2009) also find a slightly higher  $\Sigma_{10}/\langle\Sigma_{10}^{\text{cont}}\rangle$  for a sample of lower-redshift SLACS lenses compared to their twin sample, but with larger uncertainties and a lower significance. The relative overdensities of each lens are given in Table 4.

With the longer redshift baseline of the SuGOHI-g sample compared to previous lens samples, we investigate whether the relative overdensity of lens environments shows any trend with redshift. In Figure 7, we plot the normalized  $\Sigma_{10}$  values as a function of lens redshift for the individual systems. There is considerable scatter, but we fit a power law to the points using the methodology of Kelly (2007) to account for intrinsic scatter. We cannot rule out weak evolution, but the slope is still consistent with no redshift evolution in the relation.

## 6.3. Possible Sources of Systematic Error

### 6.3.1. Contamination by Stars

Although the star/galaxy classification should be reliable to  $i \sim 24$  (Aihara et al. 2018a), we check for possible contamination of our galaxy sample by interloping Milky Way stars that may not have been excluded by our extendedness cut. To do this, we plot the mean  $N_{\text{eff}}$  for a limiting magnitude of  $i = 24$  within  $r \leq 120''$  of each control field as a function of distance from the Galactic equator,  $|b|$ , in Figure 8. If there is contamination from stars, there should be higher effective number counts at lower Galactic latitude. In fact, there is no such effect, suggesting that our extendedness cut is adequately selecting galaxies.

### 6.3.2. Magnification Bias

One might suspect that since lenses reside in locally overdense environments, there may be enhancement or depletion of LOS galaxy number counts due to lensing magnification effects. The direction and size of the effect depends on the logarithmic slope of the cumulative number counts of background galaxies at the limiting magnitude being considered. For a log slope steeper than the lensing-invariant slope of  $s = 0.4$ , there should be an enhancement, while for a log slope shallower than  $s = 0.4$ , there should be a depletion (e.g., Chiu et al. 2016).

In Figure 9, we plot the cumulative number counts as a function of limiting magnitude for all galaxies within an aperture of  $r \leq 120''$  centered on the control fields that have a photometric redshift higher than the mean redshift of the lenses in our sample. We find that the log slope at  $i = 24$  is  $s = 0.40$ , which matches the lensing-invariant value, implying that magnification bias is not a significant effect. The slope steepens toward brighter limiting magnitudes, so in principle there could be a slight enhancement in the galaxy number counts at these brighter limits due to magnification effects. However, this will be diluted by lower-redshift galaxies that are either unaffected by magnification from the lens galaxy and its local environment (since they are in the foreground) or have a low lensing efficiency (since  $D_{\text{LS}}/D_S$  is small). This effect is also offset by the fact that samples of brighter objects will contain a higher fraction of objects at lower redshift.

We run a simple test to determine how large an effect lensing magnification could have. Using the GRAVELENS software (Keeton 2001), we generate a mass model consisting of an NFW halo (Navarro et al. 1997) at  $z = 0.514$ , which is the mean redshift of our main lens sample. The halo is given a mass of  $10^{14} M_\odot$ , which would represent a lens environment that is more massive than typically observed, but is still plausible given the velocity dispersion and stellar mass range of our lens sample. The halo concentration parameter for this halo mass is taken from the results of simulations by Zhao et al. (2009), and we assume an ellipticity of  $\epsilon = 0.3$ . We calculate a source-plane magnification map centered on this model for a source redshift of  $z_S = 1.0$ , which is close to the mean photometric redshift of the galaxies in the control sample that are at higher redshift than our assumed lens redshift. We then place galaxies from the control sample, which should be unbiased on average, at random locations on the source plane between  $2''.5 \leq r \leq 120''$  and calculate their apparent magnitude after being magnified. We compare the number density of galaxies in the unmagnified and magnified cases after

**Table 4**  
Local and LOS Overdensity of Individual Lens Fields

Lens	$N_{\text{eff}} / \langle N_{\text{eff}}^{\text{cont}} \rangle$ ( $r \leq 30''$ )	$N_{\text{eff}} / \langle N_{\text{eff}}^{\text{cont}} \rangle$ ( $r \leq 60''$ )	$N_{\text{eff}} / \langle N_{\text{eff}}^{\text{cont}} \rangle$ ( $r \leq 90''$ )	$N_{\text{eff}} / \langle N_{\text{eff}}^{\text{cont}} \rangle$ ( $r \leq 120''$ )	$\Sigma_{10} / \langle \Sigma_{10}^{\text{cont}} \rangle$
HSCJ015731-033057	1.33 ± 0.33	1.48 ± 0.18	1.45 ± 0.12	1.26 ± 0.08	2.37 ± 0.80
HSCJ015756-021809	1.68 ± 0.38	1.10 ± 0.15	1.02 ± 0.09	0.95 ± 0.07	0.87 ± 0.28
SDSSJ0157-0056	0.75 ± 0.23	1.00 ± 0.14	1.12 ± 0.10	1.20 ± 0.08	1.32 ± 0.43
HSCJ020141-030946	1.54 ± 0.36	1.15 ± 0.15	0.96 ± 0.09	1.02 ± 0.07	2.61 ± 0.87
HSCJ020241-064611	1.28 ± 0.32	0.95 ± 0.13	1.03 ± 0.09	1.13 ± 0.08	1.05 ± 0.34
HSCJ020846-032727	1.71 ± 0.38	1.36 ± 0.17	1.30 ± 0.11	1.33 ± 0.08	3.42 ± 1.17
SL2SJ021737-051329	1.90 ± 0.41	1.53 ± 0.18	1.19 ± 0.10	1.10 ± 0.07	4.49 ± 1.55
HSCJ022140-021020	1.26 ± 0.31	0.82 ± 0.12	0.86 ± 0.08	0.86 ± 0.06	5.02 ± 1.76
SL2SJ022315-062906	1.90 ± 0.43	1.16 ± 0.15	1.01 ± 0.09	0.91 ± 0.07	4.24 ± 1.45
SL2SJ022346-053418	1.80 ± 0.40	1.16 ± 0.15	1.06 ± 0.10	1.09 ± 0.07	2.21 ± 0.73
SL2SJ022357-065142	1.29 ± 0.31	0.98 ± 0.14	1.05 ± 0.09	1.04 ± 0.07	1.37 ± 0.45
SL2SJ022439-040045	1.35 ± 0.34	0.87 ± 0.13	0.96 ± 0.09	1.05 ± 0.07	2.06 ± 0.68
SL2SJ022511-045433	1.40 ± 0.33	1.20 ± 0.15	1.15 ± 0.10	1.10 ± 0.07	1.05 ± 0.34
SL2SJ022610-042011	1.56 ± 0.36	0.93 ± 0.13	0.91 ± 0.09	0.97 ± 0.07	1.13 ± 0.37
HSCJ023217-021703	1.21 ± 0.31	1.14 ± 0.15	1.15 ± 0.10	1.02 ± 0.07	1.11 ± 0.36
SL2SJ023307-043838	1.41 ± 0.34	1.22 ± 0.16	1.19 ± 0.10	1.11 ± 0.07	1.33 ± 0.44
HSCJ023538-063406	1.57 ± 0.36	1.06 ± 0.14	0.93 ± 0.09	0.87 ± 0.06	1.05 ± 0.34
HSCJ023637-033220	1.86 ± 0.40	1.57 ± 0.18	1.49 ± 0.12	1.36 ± 0.08	4.08 ± 1.35
HSCJ023655-023656	1.04 ± 0.28	0.97 ± 0.14	0.94 ± 0.09	0.97 ± 0.07	2.03 ± 0.67
HSCJ083943+004740	1.05 ± 0.28	1.03 ± 0.14	1.01 ± 0.09	1.10 ± 0.07	1.48 ± 0.49
HSCJ085855-010208	2.35 ± 0.48	1.22 ± 0.16	1.16 ± 0.10	1.01 ± 0.07	1.20 ± 0.39
HSCJ090507-001030	1.26 ± 0.32	0.96 ± 0.13	0.89 ± 0.09	0.93 ± 0.07	1.48 ± 0.49
HSCJ090709+005648	1.45 ± 0.34	0.92 ± 0.13	0.98 ± 0.09	0.99 ± 0.07	1.21 ± 0.40
SDSSJ0915-0055	2.61 ± 0.53	1.96 ± 0.21	1.52 ± 0.12	1.38 ± 0.09	3.22 ± 1.08
HSCJ091608+034710	1.13 ± 0.30	1.21 ± 0.16	1.09 ± 0.10	1.06 ± 0.07	3.57 ± 1.21
HSCJ091904+033638	1.47 ± 0.35	1.24 ± 0.16	1.09 ± 0.10	1.01 ± 0.07	4.57 ± 1.56
HSCJ092101+035521	1.59 ± 0.37	1.00 ± 0.14	0.83 ± 0.08	0.81 ± 0.06	1.64 ± 0.54
HSCJ093506-020031	1.42 ± 0.35	0.85 ± 0.13	0.72 ± 0.08	0.76 ± 0.06	1.21 ± 0.40
HSCJ094123+000446	1.32 ± 0.33	1.00 ± 0.14	0.94 ± 0.09	0.88 ± 0.06	1.80 ± 0.59
SDSSJ0944-0147	1.79 ± 0.40	1.64 ± 0.19	1.30 ± 0.11	1.12 ± 0.07	2.01 ± 0.66
HSCJ095750+014507	0.97 ± 0.27	0.86 ± 0.13	0.87 ± 0.09	0.91 ± 0.07	1.10 ± 0.36
COSMOS0013+2249	0.93 ± 0.26	1.09 ± 0.15	1.12 ± 0.10	1.15 ± 0.08	4.10 ± 1.38
COSMOS0056+1226	1.12 ± 0.29	0.99 ± 0.14	1.00 ± 0.09	0.99 ± 0.07	2.16 ± 0.71
HSCJ100659+024735	1.95 ± 0.42	1.28 ± 0.16	1.11 ± 0.10	1.00 ± 0.07	7.93 ± 2.83
HSCJ114311-013935	0.92 ± 0.26	0.96 ± 0.13	1.07 ± 0.10	1.14 ± 0.08	1.47 ± 0.49
HSCJ115653-003948	1.19 ± 0.30	1.36 ± 0.17	1.38 ± 0.11	1.43 ± 0.09	1.18 ± 0.38
HSCJ120623+001507	1.41 ± 0.34	1.13 ± 0.15	1.14 ± 0.10	1.22 ± 0.08	3.66 ± 1.24
HSCJ121052-011905	0.85 ± 0.25	1.06 ± 0.14	1.03 ± 0.09	1.19 ± 0.08	1.49 ± 0.49
HSCJ122048+002145	3.11 ± 0.58	2.06 ± 0.22	1.62 ± 0.13	1.52 ± 0.09	5.71 ± 1.97
HSCJ122314-002939	1.25 ± 0.33	1.32 ± 0.16	1.19 ± 0.10	1.07 ± 0.07	1.66 ± 0.55
HSCJ123825+003212	2.00 ± 0.43	1.37 ± 0.17	1.26 ± 0.11	1.18 ± 0.08	2.56 ± 0.85
HSCJ124320-004517	2.10 ± 0.45	1.40 ± 0.17	1.27 ± 0.11	1.14 ± 0.08	4.09 ± 1.41
HSCJ125254+004356	1.57 ± 0.37	1.43 ± 0.17	1.25 ± 0.11	1.08 ± 0.07	2.43 ± 0.82
HSCJ134351+010817	1.67 ± 0.38	1.51 ± 0.18	1.33 ± 0.11	1.18 ± 0.08	2.76 ± 0.93
HSCJ135038+002550	1.49 ± 0.36	1.40 ± 0.17	1.19 ± 0.10	1.03 ± 0.07	2.32 ± 0.77
HSCJ135138+002839	2.71 ± 0.54	1.46 ± 0.18	1.46 ± 0.12	1.35 ± 0.08	8.16 ± 2.92
HSCJ135242-002614	0.70 ± 0.22	0.77 ± 0.12	0.84 ± 0.08	0.93 ± 0.07	0.75 ± 0.24
HSCJ135853-021525	2.03 ± 0.44	1.37 ± 0.17	1.21 ± 0.10	1.22 ± 0.08	3.60 ± 1.23
HSCJ140929-011410	1.36 ± 0.33	1.66 ± 0.19	1.34 ± 0.11	1.27 ± 0.08	2.28 ± 0.76
HSCJ141001+012956	1.19 ± 0.30	1.12 ± 0.15	1.09 ± 0.10	1.17 ± 0.08	1.82 ± 0.60
HSCJ141300-012608	1.10 ± 0.29	0.93 ± 0.13	0.92 ± 0.09	0.97 ± 0.07	0.74 ± 0.24
HSCJ141831-000052	1.63 ± 0.37	1.59 ± 0.18	1.15 ± 0.10	1.15 ± 0.08	2.44 ± 0.80
HSCJ142353+013446	1.30 ± 0.32	1.31 ± 0.16	1.08 ± 0.10	1.11 ± 0.07	2.19 ± 0.73
HSCJ142449-005321	3.20 ± 0.61	1.79 ± 0.20	1.74 ± 0.13	1.68 ± 0.10	8.54 ± 3.16
HSCJ142720+001916	1.55 ± 0.36	1.49 ± 0.18	1.38 ± 0.11	1.31 ± 0.08	3.21 ± 1.08
HSCJ142748+000958	1.30 ± 0.32	1.36 ± 0.17	1.17 ± 0.10	1.27 ± 0.08	2.05 ± 0.68
HSCJ144307-004056	0.76 ± 0.24	1.06 ± 0.14	0.99 ± 0.09	0.96 ± 0.07	1.34 ± 0.44
HSCJ144428-005142	1.96 ± 0.42	1.26 ± 0.16	1.09 ± 0.10	1.09 ± 0.07	8.53 ± 3.10
HSCJ145236-002142	2.63 ± 0.52	1.61 ± 0.19	1.35 ± 0.11	1.18 ± 0.08	6.60 ± 2.37
HSCJ145732-015917	2.61 ± 0.53	1.48 ± 0.18	1.34 ± 0.11	1.16 ± 0.08	4.93 ± 1.71
HSCJ145759+423019	1.56 ± 0.35	1.10 ± 0.14	1.13 ± 0.10	1.11 ± 0.07	4.11 ± 1.42
HSCJ145902-012351	1.00 ± 0.27	1.01 ± 0.14	0.88 ± 0.09	1.00 ± 0.07	1.38 ± 0.45
HSCJ151336+433251	1.12 ± 0.29	1.40 ± 0.17	1.21 ± 0.10	1.13 ± 0.08	2.63 ± 0.88

**Table 4**  
(Continued)

Lens	$N_{\text{eff}} / \langle N_{\text{eff}}^{\text{cont}} \rangle$ ( $r \leq 30''$ )	$N_{\text{eff}} / \langle N_{\text{eff}}^{\text{cont}} \rangle$ ( $r \leq 60''$ )	$N_{\text{eff}} / \langle N_{\text{eff}}^{\text{cont}} \rangle$ ( $r \leq 90''$ )	$N_{\text{eff}} / \langle N_{\text{eff}}^{\text{cont}} \rangle$ ( $r \leq 120''$ )	$\Sigma_{10} / \langle \Sigma_{10}^{\text{cont}} \rangle$
HSCJ155826+432830	$1.35 \pm 0.34$	$1.07 \pm 0.14$	$0.93 \pm 0.09$	$1.02 \pm 0.07$	$1.04 \pm 0.34$
SL2SJ220202+014710	$0.78 \pm 0.24$	$0.67 \pm 0.11$	$0.84 \pm 0.08$	$0.88 \pm 0.06$	$0.86 \pm 0.28$
SL2SJ220506+014703	$2.22 \pm 0.47$	$1.69 \pm 0.20$	$1.45 \pm 0.12$	$1.35 \pm 0.09$	$1.83 \pm 0.60$
HSCJ220550+041524	$1.81 \pm 0.40$	$1.38 \pm 0.17$	$1.27 \pm 0.11$	$1.20 \pm 0.08$	$2.07 \pm 0.67$
SL2SJ220642+041131	$1.79 \pm 0.40$	$1.34 \pm 0.16$	$1.07 \pm 0.10$	$1.00 \pm 0.07$	$5.17 \pm 1.82$
HSCJ221726+000350	$1.16 \pm 0.30$	$1.09 \pm 0.15$	$1.01 \pm 0.09$	$0.91 \pm 0.07$	$7.10 \pm 2.48$
SL2SJ221852+014038	$1.06 \pm 0.29$	$1.04 \pm 0.14$	$0.93 \pm 0.09$	$1.00 \pm 0.07$	$1.62 \pm 0.53$
HSCJ222801+012805	$1.10 \pm 0.29$	$1.00 \pm 0.14$	$1.02 \pm 0.09$	$1.11 \pm 0.07$	$1.36 \pm 0.45$
HSCJ223518-004747	$1.16 \pm 0.30$	$1.14 \pm 0.15$	$1.13 \pm 0.10$	$1.09 \pm 0.07$	$4.38 \pm 1.52$
HSCJ223733+005015	$0.83 \pm 0.25$	$1.06 \pm 0.14$	$0.95 \pm 0.09$	$0.96 \pm 0.07$	$1.33 \pm 0.44$
HSCJ224201+022810	$1.51 \pm 0.36$	$0.98 \pm 0.14$	$0.90 \pm 0.09$	$1.05 \pm 0.07$	$1.28 \pm 0.42$
HSCJ224221+001144	$1.14 \pm 0.30$	$0.95 \pm 0.13$	$1.21 \pm 0.10$	$1.18 \pm 0.08$	$2.81 \pm 0.93$
HSCJ224454+031551	$1.29 \pm 0.32$	$1.11 \pm 0.15$	$1.01 \pm 0.09$	$1.03 \pm 0.07$	$1.39 \pm 0.46$
HSCJ224800-010259	$1.34 \pm 0.33$	$1.19 \pm 0.15$	$1.22 \pm 0.11$	$1.04 \pm 0.07$	$1.64 \pm 0.53$
HSCJ225800+004533	$1.02 \pm 0.28$	$1.30 \pm 0.16$	$1.19 \pm 0.10$	$1.14 \pm 0.08$	$1.93 \pm 0.64$
SDSSJ2303+0037	$1.96 \pm 0.43$	$1.30 \pm 0.16$	$1.16 \pm 0.10$	$1.11 \pm 0.07$	$3.17 \pm 1.06$
HSCJ230521-000211	$1.59 \pm 0.36$	$1.08 \pm 0.14$	$0.89 \pm 0.09$	$0.87 \pm 0.06$	$1.42 \pm 0.46$
HSCJ231004+024759	$3.30 \pm 0.63$	$2.00 \pm 0.22$	$1.71 \pm 0.13$	$1.50 \pm 0.09$	$10.29 \pm 3.68$
HSCJ231145-013039	$1.61 \pm 0.36$	$1.14 \pm 0.15$	$1.02 \pm 0.09$	$1.02 \pm 0.07$	$1.99 \pm 0.66$
HSCJ232415+011331	$1.04 \pm 0.28$	$0.95 \pm 0.13$	$1.02 \pm 0.09$	$1.16 \pm 0.08$	$1.80 \pm 0.59$
HSCJ233130+003733	$1.39 \pm 0.33$	$1.14 \pm 0.15$	$1.33 \pm 0.11$	$1.39 \pm 0.09$	$1.41 \pm 0.46$
HSCJ233146+013845	$1.44 \pm 0.34$	$1.15 \pm 0.15$	$1.11 \pm 0.10$	$1.05 \pm 0.07$	$3.48 \pm 1.17$
HSCJ233311+022310	$1.06 \pm 0.28$	$0.91 \pm 0.13$	$0.98 \pm 0.09$	$0.89 \pm 0.07$	$1.07 \pm 0.35$
HSCJ233528+001355	$1.75 \pm 0.39$	$1.32 \pm 0.16$	$1.15 \pm 0.10$	$1.24 \pm 0.08$	$4.01 \pm 1.37$

**Note.** Relative LOS overdensities are calculated for a magnitude limit of  $i \leq 24$ . Overdensities are normalized by the mean values across all control fields. The uncertainties include Poisson uncertainties in the calculation of lens field quantities and error on the mean in the control fields.

accounting for depletion of source area in the fixed aperture due to lensing. We find that even in this aggressive scenario that represents a rich lens environment, the typical effect is a  $< 1\%$  change in number counts at  $i \leq 23$ , with a likely comparable change at  $i \leq 24$  given the relatively constant slope in Figure 9. We repeat this test for a  $10^{15} M_{\odot}$  halo, which represents an extreme cluster environment, and find a similarly small enhancement. We therefore conclude that the effect of magnification bias on galaxy number counts is negligible in the context of this study, although we cannot necessarily extend this to deeper surveys or lens samples with a significantly different redshift distribution.

### 6.3.3. Effect of Photometric Redshift Outliers

The photometric redshifts used in our analysis have a scatter and a possibility of catastrophic outliers, as described in Section 2.1. Since lenses reside in locally overdense environments, we intuitively expect that redshift outliers will lead to an underestimate of the local overdensity of lens galaxies since more galaxies will scatter out of the lens plane than will scatter into it. To demonstrate this, we show a simple model.

For a given lens at a redshift  $z_L$ , let  $N_{z=z_L}^{\text{lens}}$  and  $N_{z \neq z_L}^{\text{lens}}$  be the number of objects in the lens plane and along the LOS, respectively, in the lens field. Similarly, let  $N_{z=z_L}^{\text{cont}}$  and  $N_{z \neq z_L}^{\text{cont}}$  be the number of objects in the lens plane and along the LOS, respectively, in a control field. The total number counts in the lens field is then  $N^{\text{lens}} = N_{z=z_L}^{\text{lens}} + N_{z \neq z_L}^{\text{lens}}$  and the total number counts in the control field is  $N^{\text{cont}} = N_{z=z_L}^{\text{cont}} + N_{z \neq z_L}^{\text{cont}}$ .

We then allow for photometric redshift outliers and assume that the global outlier rate applies to both the lens and control fields. Let  $f_{\text{in}}$  be the fraction of LOS galaxies that scatter into

the lens plane, and  $f_{\text{out}}$  be the fraction of galaxies in the lens plane that scatter out of the lens plane and into the LOS. Our intuitive conjecture is that the measured relative overdensity is smaller than the true overdensity. In other words, we expect that

$$\frac{(1 - f_{\text{out}})N_{z=z_L}^{\text{lens}} + f_{\text{in}}N_{z \neq z_L}^{\text{lens}}}{(1 - f_{\text{out}})N_{z=z_L}^{\text{cont}} + f_{\text{in}}N_{z \neq z_L}^{\text{cont}}} < \frac{N_{z=z_L}^{\text{lens}}}{N_{z=z_L}^{\text{cont}}}. \quad (4)$$

Multiplying through Equation (4) by the denominators of both sides and eliminating common factors, this simplifies to

$$N_{z \neq z_L}^{\text{lens}} N_{z=z_L}^{\text{cont}} < N_{z \neq z_L}^{\text{cont}} N_{z=z_L}^{\text{lens}}. \quad (5)$$

Rearranging to separate the lens field and control field quantities, we get

$$\frac{N_{z=z_L}^{\text{cont}}}{N_{z \neq z_L}^{\text{cont}}} < \frac{N_{z=z_L}^{\text{lens}}}{N_{z \neq z_L}^{\text{lens}}}. \quad (6)$$

Equation (6) is simply the statement that lenses lie in locally overdense redshift planes relative to a random control field, which our results have already demonstrated. Therefore, our conjecture that photometric redshift outliers will lead to an underestimate of the relative local overdensity of lenses is true, making our results conservative.

Conversely, this means that there will be a bias in the calculation of  $N_{\text{eff}}^{\text{LOS}}$  such that lens and twin fields will have slightly higher measured values compared to the control sample, i.e., the fact that Equation (4) is true necessarily

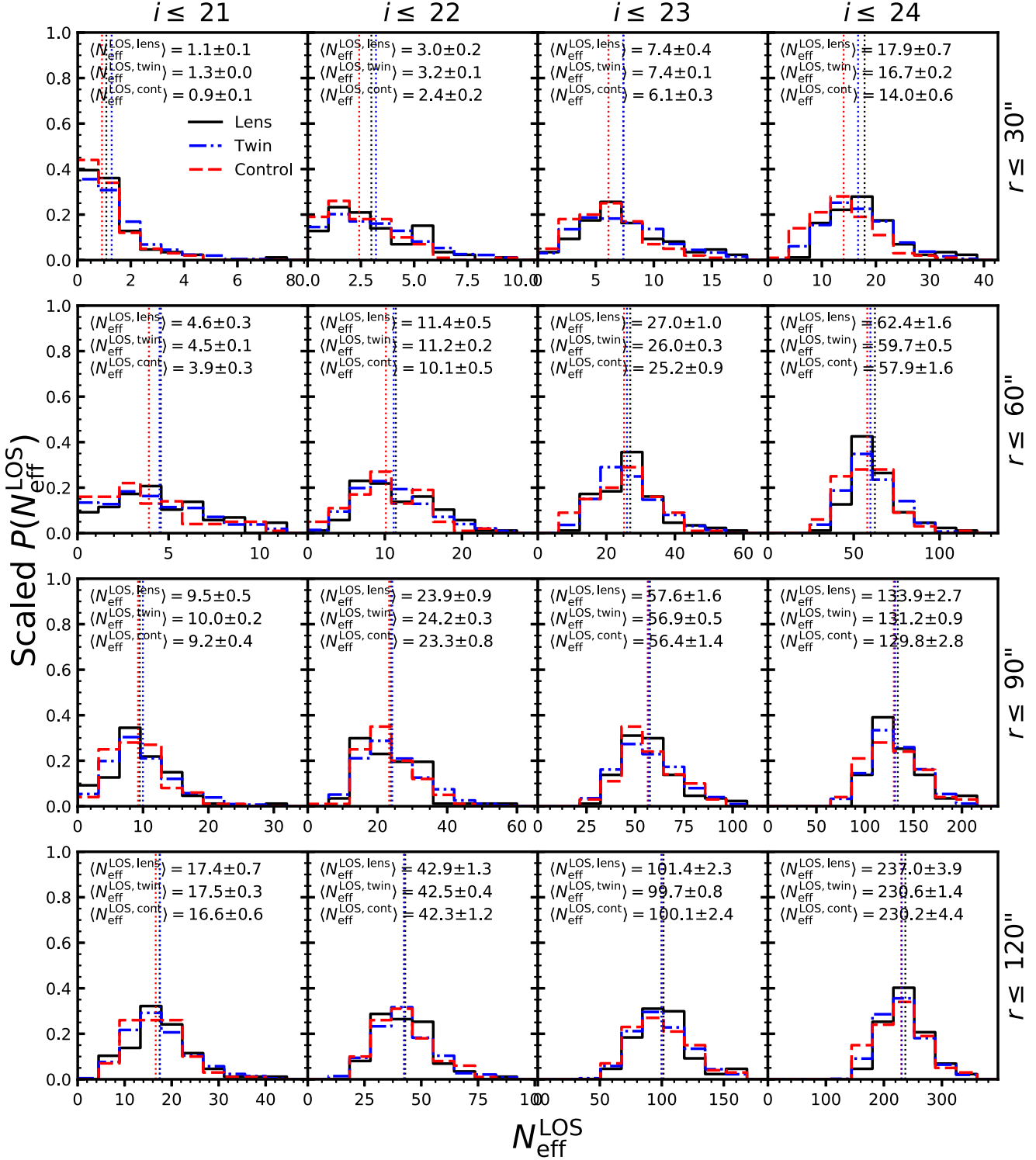


**Figure 5.** As in Figure 4, but with galaxies in the lens plane removed from the lens and twin samples, and an equivalent cut made for the control sample by randomly drawing lens redshifts for each control field. The three samples are now generally consistent, indicating that lenses do not lie along biased LOSs once the local environment has been accounted for. There is still an excess in the lens and twin samples in the smallest  $r_{\text{ap}}$  bin. We discuss a possible origin of this effect in Section 6.3.3.

means that

$$\frac{(1 - f_{\text{in}})N_{z \neq z_L}^{\text{lens}} + f_{\text{out}}N_{z=z_L}^{\text{lens}}}{(1 - f_{\text{in}})N_{z \neq z_L}^{\text{cont}} + f_{\text{out}}N_{z=z_L}^{\text{cont}}} > \frac{N_{z \neq z_L}^{\text{lens}}}{N_{z \neq z_L}^{\text{cont}}}. \quad (7)$$

To estimate the magnitude of this effect, we first define  $y$  to be the true overdensity in the lens plane,

$$y \equiv \frac{N_{z=z_L}^{\text{lens}}}{N_{z=z_L}^{\text{cont}}}. \quad (8)$$

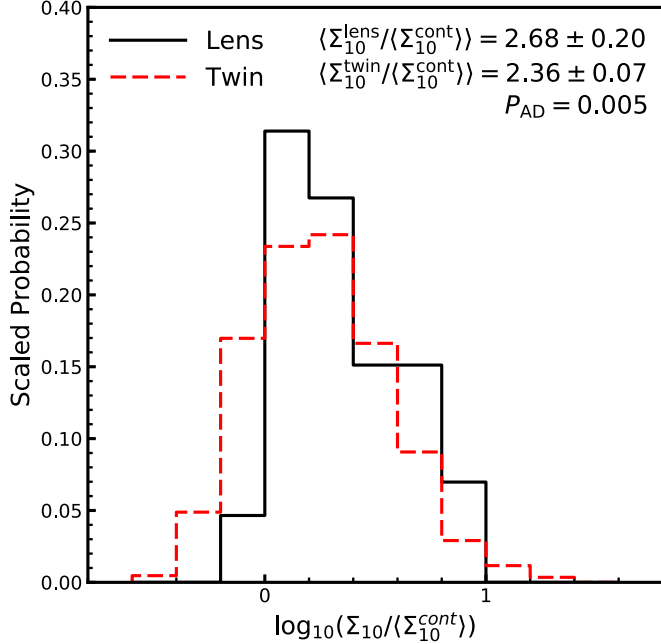


**Figure 6.** Normalized histogram of  $\Sigma_{10}$  distributions for the lens (black solid line) and twin (red dashed line) samples. The mean and standard error of each distribution is given in the upper right corner, along with the  $P_{\text{AD}}$  value. The lens galaxies have a slightly higher local overdensity than the twin galaxies, although the significance is marginal.

**Table 5**  
Two-sample Anderson–Darling Test Significance Levels—Lens Plane Removed

Lens-control				
$r$ (arcsec)	$i \leq 21$	$i \leq 22$	$i \leq 23$	$i \leq 24$
30	7.0e–01	5.2e–02	3.0e–02	<b>8.5e–05</b>
60	8.6e–02	1.8e–01	3.6e–01	2.0e–02
90	8.0e–01	9.1e–01	7.3e–01	1.7e–01
120	3.5e–01	7.1e–01	2.0e–01	1.4e–01
Lens-twin				
$r$ (arcsec)	$i \leq 21$	$i \leq 22$	$i \leq 23$	$i \leq 24$
30	4.1e–01	7.1e–01	9.8e–01	1.8e–01
60	6.0e–01	8.4e–01	5.0e–01	1.4e–01
90	5.0e–01	5.5e–01	4.6e–01	4.5e–01
120	6.4e–01	6.8e–01	2.5e–01	1.3e–01
Twin-control				
$r$ (arcsec)	$i \leq 21$	$i \leq 22$	$i \leq 23$	$i \leq 24$
30	2.2e–02	<b>2.2e–03</b>	<b>2.2e–03</b>	<b>9.6e–05</b>
60	1.2e–01	1.2e–01	4.0e–01	1.5e–01
90	2.5e–01	4.9e–01	9.0e–01	4.7e–01
120	3.4e–01	1.0e+00	7.6e–01	7.4e–01

**Note.** The values represent  $P_{\text{AD}}$ , the significance level at which the null hypothesis that the samples are drawn from the same parent distribution can be rejected. Values in italics are significant at greater than the  $2\sigma$  level, while values in bold are significant at greater than the  $3\sigma$  level.

For small  $\Delta z / (1 + z_L)$ , we can make the approximation  $f_{\text{in}} \approx 0$  because the total outlier fraction for LOS galaxies is small (of order  $\sim 0.1$ ) and the likelihood of an outlier scattering into the lens plane is small (of order

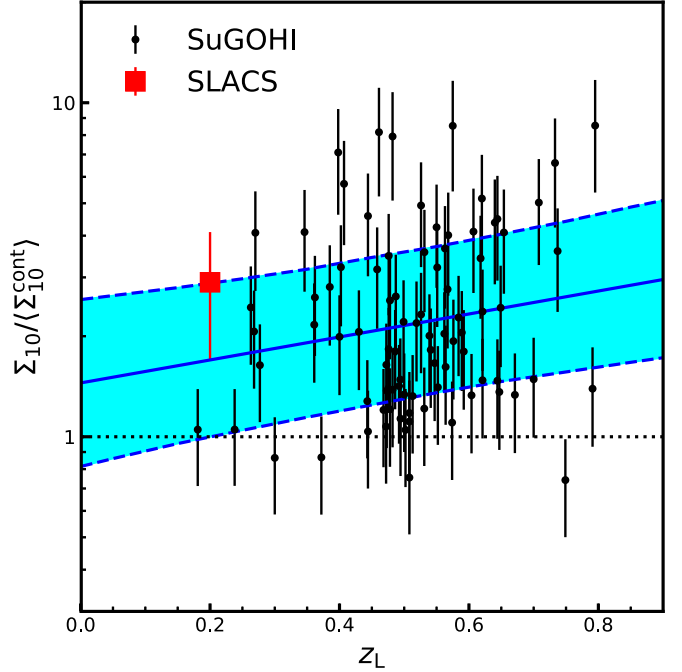


**Figure 7.** Normalized  $\Sigma_{10}$  distributions for the individual SuGOHI-g lenses (black points) as a function of lens redshift. The black dotted line represents a density equal to that of a random field. For comparison, we plot the SLACS result of Treu et al. (2009) at the mean redshift of their sample (red square), although we note that they use a variable magnitude cut, so their results may not be exactly analogous to ours. The blue line and shaded region represent the best-fit power-law relation and 68% pointwise confidence interval using the methodology of Kelly (2007). We cannot rule out weak evolution, but the slope is still consistent with no redshift evolution in the relation.

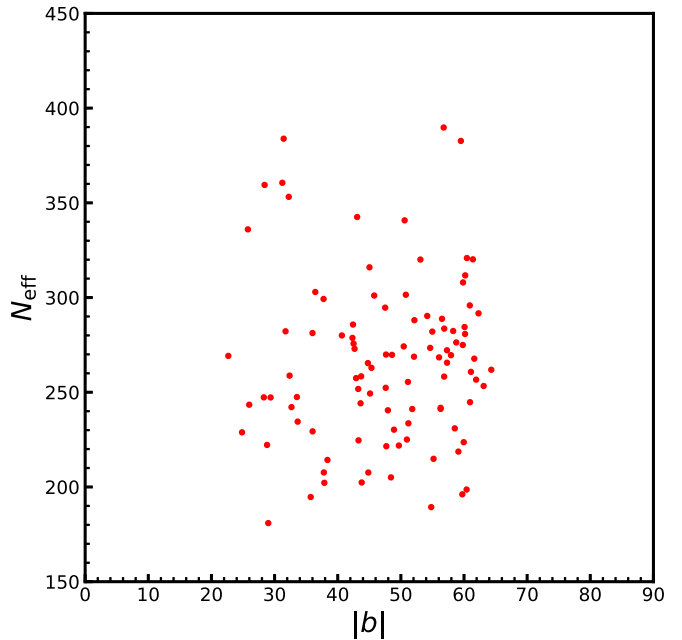


**Figure 8.** Mean  $N_{\text{eff}}$  for a limiting magnitude of  $i = 24$  within  $r \leq 120''$  of each control field as a function of distance from the Galactic equator,  $|b|$ . The effective number counts are not systematically higher at low Galactic latitudes, suggesting that our extendedness cut is adequately selecting galaxies.

$\sim \Delta z / (1 + z_L) \sim 0.1$ , so their product is small. We can then define  $x$  to be the measured LOS overdensity (the left-hand side of Equation (7)) under this

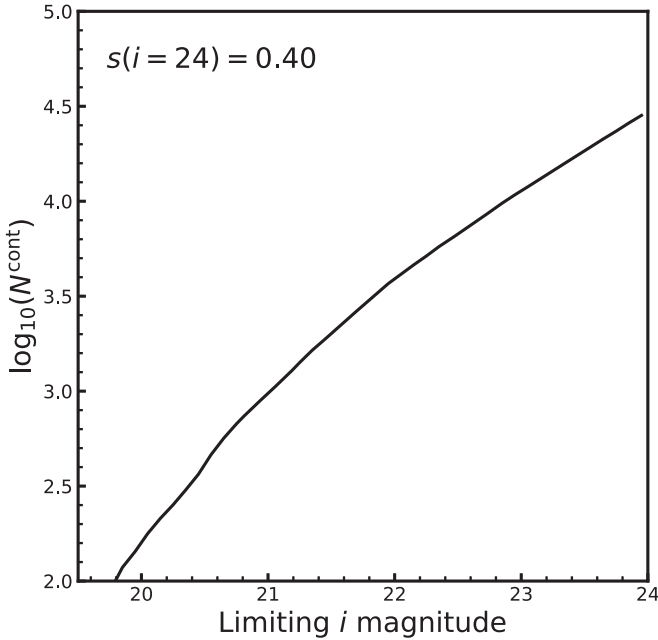


**Figure 9.** Cumulative number counts as a function of limiting magnitude for all galaxies within an aperture of  $r \leq 120''$  centered on the control fields that have a photometric redshift higher than the mean redshift of the lens sample,  $z \geq 0.514$ . The logarithmic slope of the cumulative number counts at  $i = 24$  is  $s = 0.40$ . This matches the lensing-invariant slope of  $s = 0.4$ , meaning that any magnification bias arising from overdensities associated with the lens environment should have a minimal effect.

approximation:

$$x \equiv \frac{N_{z \neq z_L}^{\text{lens}} + f_{\text{out}} N_{z=z_L}^{\text{lens}}}{N_{z \neq z_L}^{\text{cont}} + f_{\text{out}} N_{z=z_L}^{\text{cont}}} \quad (9)$$

$$= \frac{N_{z \neq z_L}^{\text{lens}} + y f_{\text{out}} N_{z=z_L}^{\text{cont}}}{N_{z \neq z_L}^{\text{cont}} + f_{\text{out}} N_{z=z_L}^{\text{cont}}}. \quad (10)$$

We can then rearrange Equation (10) to calculate the true LOS overdensity,

$$\frac{N_{z \neq z_L}^{\text{lens}}}{N_{z \neq z_L}^{\text{cont}}} = x - f_{\text{out}} \frac{N_{z=z_L}^{\text{cont}}}{N_{z \neq z_L}^{\text{cont}}} (y - x). \quad (11)$$

where  $f_{\text{out}}$  should be similar to the global value of galaxies that scatter beyond  $\Delta z/(1+z_L) = 0.05$  and, given the typical 1 $\sigma$  redshift scatter, is approximately  $f_{\text{out}} \approx 0.3$ ,  $N_{z=z_L}^{\text{cont}}/N_{z \neq z_L}^{\text{cont}}$  is the ratio of number counts in the lens plane to number counts in the LOS for the control field and can be estimated from the fractional difference in the distributions for a given magnitude and aperture cut between Figures 4 and 5; this roughly gives  $N_{z=z_L}^{\text{cont}}/N_{z \neq z_L}^{\text{cont}} \approx 0.2$ . The factor  $y$  can be estimated from Figures 4 and 5 for a given magnitude and aperture cut and is generally in the range  $1.5 \lesssim y \lesssim 2$ , and  $x \approx 1$ , thus  $0.5 \lesssim (y - x) \lesssim 1$ . Therefore, the bias due to photometric redshift outliers is a few percent, which may explain the statistically similar but consistently larger LOS overdensities in the lens fields relative to the control fields in Figure 5.

#### 6.3.4. Magnitude-dependent Clustering Effects

Our adoption of a simple magnitude cut may lead to a systematic effect in our calculation of the relative overdensities

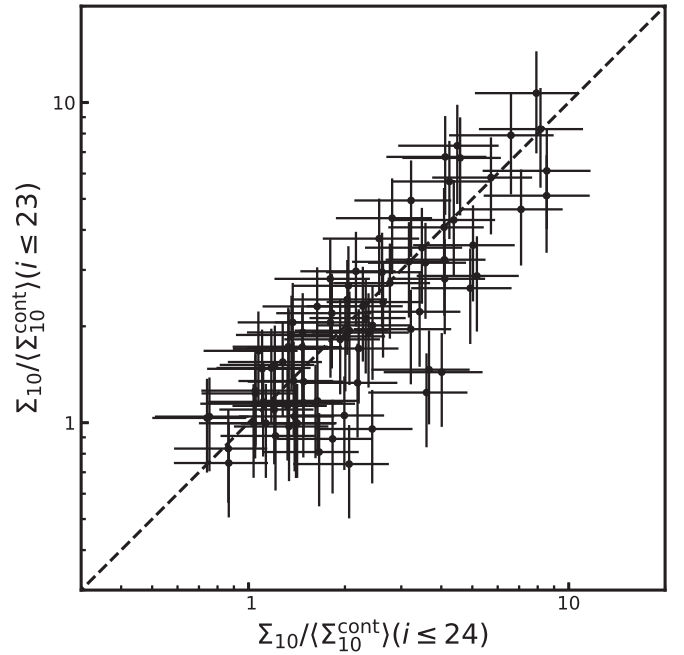


**Figure 10.** Normalized  $\Sigma_{10}$  distributions for individual SuGOHI-g lenses calculated using galaxies brighter than  $i \leq 23$  as a function of the same quantity calculated using galaxies brighter than  $i \leq 24$ . Most of the normalized  $\Sigma_{10}$  values remain consistent within the uncertainties, and there is no systematic trend toward higher overdensities. Therefore, there does not appear to be a bias arising from our choice of magnitude cut.

of the local lens environments. Although our normalization of  $\Sigma_{10}$  by the average density of the control fields for an equivalent redshift slice should mitigate this, there could still be a second-order effect since galaxy clustering strength is known to be stronger for brighter and more massive galaxies (e.g., Zehavi et al. 2005).

In Figure 10, we plot the relative overdensities of our lens sample against the same quantity calculated using galaxies at  $i \leq 23$ . When calculated with the brighter magnitude limit, most of the relative overdensities remain consistent within the uncertainties, and there is no systematic trend toward higher overdensities. Therefore, there does not appear to be a bias arising from our choice of magnitude cut.

## 7. Conclusions

We have presented newly discovered SuGOHI-g lens candidates from Data Release 2 of the HSC SSP. In total, we find 41 promising new candidates, comprising 7 “definite” (grade A) lenses and 34 “probable” (grade B) lenses.

Using these data, along with previously known and discovered lenses in the survey, we have studied LOSs of 87 strong gravitational lens galaxies to investigate whether they are overdense in comparison to random LOSs in the universe. This study improves on a past analysis by Fassnacht et al. (2011) by taking advantage of the substantial area and multiband nature of the HSC SSP, which allows us to use photometric redshifts to accurately distinguish galaxies in the local lens environment from LOS galaxies in projection. Our results are in agreement with Fassnacht et al. (2011) in that lens galaxies lie in overdense LOS compared to randomly chosen lines of sight, but this effect can be explained by the overdense local environments of lenses. Once the galaxies in the lens plane are removed, the lens LOS overdensities are consistent with the control sample. There may be a

magnification bias due to the overdense lens environments, but the effect is likely small and is not strong enough to influence our results. Photometric redshift scatter can lead to a slight overestimate of the lens fields' LOS number counts, but this is likely to be only a few percent.

We have also investigated the local environments of lens galaxies by comparing them to both a random control sample and a sample of “twin” galaxies that are matched in redshift and velocity dispersion. This extends the work of Treu et al. (2009) who used the SLACS sample that had a mean lens redshift of  $z_L = 0.2$ , out to a redshift of  $z_L = 0.8$ . We find that lenses have denser local environments than random fields at the same redshift. There is an indication that their environments are slightly more dense than the twin galaxies, although the statistical significance is marginal, in agreement with Treu et al. (2009). A bias in the velocity dispersion measurements of the lens galaxies may explain this result, but higher-precision velocity dispersion measurements are needed for confirmation. There is no evidence for redshift evolution in the relative overdensity of lens environments.

We have calculated the local and LOS relative overdensities for known galaxy-scale lenses in the HSC SSP through Data Release 2. These quantities will be valuable for evaluating the potential effects of external structure and biases that can arise in lens modeling from those effects, as well as for studying the relationship between the environments of lens galaxies and their physical properties as inferred from lens modeling. This work will also inform future studies of this lens sample in terms of follow-up strategies and prioritizing optimal targets.

We thank the referee, whose feedback and suggestions were helpful in improving this paper. We thank Jean Coupon for help with the HSC SSP bright star masks and random object catalog. We thank Chris Fassnacht for providing us with his galaxy catalog to directly compare number counts in overlapping fields. The Hyper Suprime-Cam (HSC) collaboration includes the astronomical communities of Japan and Taiwan, and Princeton University. The HSC instrumentation and software were developed by the National Astronomical Observatory of Japan (NAOJ), the Kavli Institute for the Physics and Mathematics of the Universe (Kavli IPMU), the University of Tokyo, the High Energy Accelerator Research Organization (KEK), the Academia Sinica Institute for Astronomy and Astrophysics in Taiwan (ASIAA), and Princeton University. Funding was contributed by the FIRST program from Japanese Cabinet Office, the Ministry of Education, Culture, Sports, Science and Technology (MEXT), the Japan Society for the Promotion of Science (JSPS), Japan Science and Technology Agency (JST), the Toray Science Foundation, NAOJ, Kavli IPMU, KEK, ASIAA, and Princeton University. This work is based in part on data collected at the Subaru Telescope and retrieved from the HSC data archive system, which is operated by the Subaru Telescope and Astronomy Data Center at National Astronomical Observatory of Japan. Funding for SDSS-III has been provided by the Alfred P. Sloan Foundation, the Participating Institutions, the National Science Foundation, and the U.S. Department of Energy Office of Science. The SDSS-III website is <http://www.sdss3.org/>. SDSS-III is managed by the Astrophysical Research Consortium for the Participating Institutions of the SDSS-III Collaboration including the University of Arizona, the Brazilian Participation Group, Brookhaven National

Laboratory, Carnegie Mellon University, University of Florida, the French Participation Group, the German Participation Group, Harvard University, the Instituto de Astrofísica de Canarias, the Michigan State/Notre Dame/JINA Participation Group, Johns Hopkins University, Lawrence Berkeley National Laboratory, Max Planck Institute for Astrophysics, Max Planck Institute for Extraterrestrial Physics, New Mexico State University, New York University, Ohio State University, Pennsylvania State University, University of Portsmouth, Princeton University, the Spanish Participation Group, University of Tokyo, University of Utah, Vanderbilt University, University of Virginia, University of Washington, and Yale University. K.C.W. is supported by an EACOA Fellowship awarded by the East Asia Core Observatories Association, which consists of the Academia Sinica Institute of Astronomy and Astrophysics, the National Astronomical Observatory of Japan, the National Astronomical Observatories of the Chinese Academy of Sciences, and the Korea Astronomy and Space Science Institute. This work was supported in part by World Premier International Research Center Initiative (WPI Initiative), MEXT, Japan, and JSPS KAKENHI Grant Number JP15H05892, and JP18K03693. S.H.S. thanks the Max Planck Society for support through the Max Planck Research Group.

## Appendix A Lenses Not in the Main Sample and Comparison with Previous Studies

Some known lenses are not included in our main sample because they either do not have BOSS spectroscopy or do not have reliable velocity dispersion measurements from BOSS (Section 4.1), so we cannot select a sample of twin galaxies for them. There may also be previously known lenses that are contained within the survey area, but that were not in the lens selection function. These lenses are listed in Table 6. However, we can still calculate  $N_{\text{eff}}$  and the local environment overdensity for these systems. For completeness, we present these results in Table 7. Although these systems could have been used in the parts of our analysis that did not make a direct comparison to the twin sample, we exclude them in order to maintain a consistent main sample throughout. Some of these lenses (as well as some lenses in the main sample) may also have independent velocity dispersion measurements, but for consistency, we only use the velocity dispersions from BOSS.

We note that two lenses outside of our main sample, SDSS J0924+0219 and SDSS J1226–0006, are also in the Fassnacht et al. (2011) sample. Our calculated relative LOS overdensity is consistent with theirs for SDSS J1226–0006, but slightly lower than their value (1.20 in a 45'' radius aperture) for SDSS J0924 +0219, although their errors are likely large due to their small control sample. The Fassnacht et al. (2011) study goes to a deeper limiting magnitude of  $m_{\text{F814W}} \leq 24.25$  on the Vega magnitude system, which could also affect the number counts (C. Fassnacht 2018, private communication).

Among our entire sample (including those outside the main sample), there are eight lenses that overlap the Treu et al. (2009) SLACS sample. Our calculated relative local overdensities for six of those systems are consistent with their results within the  $1\sigma$  uncertainties. Of the two systems where our results do not agree, SDSS J0935–0003 is consistent within  $2\sigma$ , and SDSS J1250 –0135 is in a dense cluster environment at a low redshift of  $z = 0.087$  where the MIZUKI photometric redshifts have a higher catastrophic outlier rate (Tanaka et al. 2018).

**Table 6**  
Additional Lenses Not in Main Sample

Lens	$\alpha$ (J2000)	$\delta$ (J2000)	$z_L$	$z_S$	Reference <sup>a</sup>
SL2SJ021247–055552	33.1993	−5.9312	0.750	2.74	Sonnenfeld et al. (2013a)
SL2SJ021411–040502	33.5467	−4.0841	0.608	1.880	Sonnenfeld et al. (2013a)
SL2SJ022056–063934	35.2358	−6.6595	0.330	...	Sonnenfeld et al. (2013a)
SL2SJ022459–040104	36.2469	−4.0177	0.800	...	More et al. (2012)
SL2SJ022648–040610	36.7016	−4.1029	0.766	...	Sonnenfeld et al. (2013a)
SL2SJ023251–040823	38.2149	−4.1399	0.352	2.344	Sonnenfeld et al. (2013a)
SDSSJ023740.63–064112.9	39.4193	−6.6869	0.486	2.2491	Shu et al. (2016)
SL2SJ085540–014730	133.9171	−1.7917	0.365	3.39	Sonnenfeld et al. (2013a)
SL2SJ085826–014300	134.6108	−1.7168	0.580	...	Sonnenfeld et al. (2013a)
SL2SJ090408–005953	136.0332	−0.9980	0.611	2.36	Sonnenfeld et al. (2013a)
HSCJ090613+032939	136.5548	3.4944	0.617	...	SuGOHI I
H-ATLASJ090740.0–004200	136.9167	−0.7000	0.613	1.5747	Negrello et al. (2010), Wong et al. (2017a)
SDSSJ0912+0029	138.0221	0.4837	0.164	0.324	Bolton et al. (2006)
SDSSJ0924+0219	141.2325	2.3236	0.394	1.524	Inada et al. (2003), Eigenbrod et al. (2006)
SDSSJ0935–0003	143.9331	−0.0597	0.347	0.467	Bolton et al. (2008)
BRI0952–0115	148.7500	−1.5014	0.632	4.5	McMahon et al. (1992), Eigenbrod et al. (2007)
SDSSJ0955+0101	148.8322	1.0290	0.111	0.316	Bolton et al. (2008)
COSMOS5914+1219	149.7696	2.2053	1.130	...	Faure et al. (2008)
COSMOS5921+0638	149.8407	2.1107	0.552	3.35	Faure et al. (2008), Sonnenfeld et al. (2013a)
J095930.93+023427.7	149.8789	2.5744	0.892	...	Faure et al. (2011)
COSMOS5939+3044	149.9132	2.5122	0.740	...	Faure et al. (2008), More et al. (2012)
COSMOS0012+2015	150.0525	2.3375	0.378	...	Faure et al. (2011)
COSMOS0018+3845	150.0767	2.6458	0.976	3.96	Faure et al. (2011)
COSMOS0038+4133	150.1595	2.6927	0.738	...	Faure et al. (2011)
COSMOS0047+5023	150.1983	1.8397	0.870	...	Faure et al. (2011)
COSMOS0049+5128	150.2053	1.8578	0.337	0.524	Faure et al. (2011)
COSMOS0050+4901	150.2110	2.8172	0.960	...	Faure et al. (2011)
J100140.12+020040.9	150.4172	2.0114	0.879	...	Faure et al. (2011)
SL2SJ100148+022207	150.4491	2.3685	0.690	...	More et al. (2012)
COSMOS0211+1139	150.5467	2.1943	0.920	...	Faure et al. (2011), More et al. (2012)
SL2SJ100212+022955	150.5486	2.4987	0.770	...	More et al. (2012)
SL2SJ100215+023736	150.5619	2.6268	0.650	...	More et al. (2012)
COSMOS0254+1430	150.7253	2.2417	0.417	0.779	Faure et al. (2011)
SDSSJ1143–0144	175.8735	−1.7417	0.106	0.402	Bolton et al. (2008)
HSTJ114331.46–014508.0	175.8811	−1.7522	0.104	0.91	Newton et al. (2009)
SDSSJ1159–0007	179.9360	−0.1245	0.579	1.346	Brownstein et al. (2012)
SDSSJ1215+0047	183.7685	0.7906	0.642	1.297	Brownstein et al. (2012)
SDSSJ1226–0006	186.5334	−0.1006	0.516	1.1229	Eigenbrod et al. (2006), Inada et al. (2008)
SDSSJ1250–0135	192.7105	−1.5921	0.087	0.353	Bolton et al. (2008)
SDSSJ1347–0101	206.7707	−1.0176	0.397	0.63	Auger et al. (2011)
SDSSJ1403+0006	210.8729	0.1115	0.189	0.473	Bolton et al. (2008)
HSCJ141635+010128	214.1476	1.0247	0.700	...	SuGOHI I
HSCJ142053+005620	215.2234	0.9391	0.616	...	SuGOHI I
SDSSJ1436–0000	219.1148	−0.0081	0.285	0.805	Bolton et al. (2008)
SDSSJ1524+4409	231.1901	44.1638	0.320	1.21	Oguri et al. (2008)
HSCJ155319+431824	238.3308	43.3068	0.629	...	SuGOHI I
B1600+434	240.4167	43.2799	0.414	1.589	Jackson et al. (1995), Fassnacht & Cohen (1998)
SL2SJ220629+005728	331.6225	0.9580	0.704	...	Sonnenfeld et al. (2013a)
SL2SJ221326–000946	333.3591	−0.1629	0.338	3.447	Sonnenfeld et al. (2013a)
SL2SJ221929–001743	334.8725	−0.2954	0.289	1.023	Sonnenfeld et al. (2013a)
SL2SJ222148+011542	335.4534	1.2619	0.325	2.35	Sonnenfeld et al. (2013a)
SL2SJ222217+001202	335.5735	0.2008	0.436	1.36	Sonnenfeld et al. (2013a)
Q2237+0305	340.1250	3.3580	0.039	1.695	Huchra et al. (1985)
SDSSJ2300+0022	345.2214	0.3772	0.228	0.463	Bolton et al. (2006)
HSCJ233230+003821	353.1289	0.6394	0.623	...	SuGOHI II

**Notes.** Lenses listed here either do not have velocity dispersion measurements from BOSS or have unreliable velocity dispersion measurements, so they are not included in our main analysis.

<sup>a</sup> SuGOHI I = Sonnenfeld et al. (2018); SuGOHI II = this work.

**Table 7**  
Local and LOS Overdensity of Individual Lens Fields Not in Main Sample

Lens	$N_{\text{eff}} / \langle N_{\text{eff}}^{\text{cont}} \rangle$ ( $r \leq 30''$ )	$N_{\text{eff}} / \langle N_{\text{eff}}^{\text{cont}} \rangle$ ( $r \leq 60''$ )	$N_{\text{eff}} / \langle N_{\text{eff}}^{\text{cont}} \rangle$ ( $r \leq 90''$ )	$N_{\text{eff}} / \langle N_{\text{eff}}^{\text{cont}} \rangle$ ( $r \leq 120''$ )	$\Sigma_{10} / \langle \Sigma_{10}^{\text{cont}} \rangle$
SL2SJ021247–055552	$1.30 \pm 0.32$	$0.95 \pm 0.13$	$1.11 \pm 0.10$	$1.25 \pm 0.08$	$2.74 \pm 0.92$
SL2SJ021411–040502	$1.85 \pm 0.41$	$1.34 \pm 0.17$	$1.20 \pm 0.10$	$1.13 \pm 0.08$	$4.18 \pm 1.44$
SL2SJ022056–063934	$0.30 \pm 0.14$	$0.73 \pm 0.11$	$0.77 \pm 0.08$	$0.88 \pm 0.06$	$0.68 \pm 0.22$
SL2SJ022459–040104	$0.84 \pm 0.25$	$0.97 \pm 0.13$	$0.98 \pm 0.09$	$0.94 \pm 0.07$	$0.78 \pm 0.25$
SL2SJ022648–040610	$1.40 \pm 0.34$	$0.97 \pm 0.14$	$0.94 \pm 0.09$	$1.05 \pm 0.07$	$1.94 \pm 0.65$
SL2SJ023251–040823	$1.80 \pm 0.40$	$1.08 \pm 0.14$	$1.03 \pm 0.09$	$1.05 \pm 0.07$	$1.58 \pm 0.52$
SDSSJ023740.63–064112.9	$0.77 \pm 0.23$	$0.75 \pm 0.12$	$0.85 \pm 0.08$	$0.82 \pm 0.06$	$0.95 \pm 0.31$
SL2SJ085540–014730	$1.30 \pm 0.32$	$1.17 \pm 0.15$	$1.25 \pm 0.11$	$1.02 \pm 0.07$	$1.34 \pm 0.44$
SL2SJ085826–014300	$1.35 \pm 0.33$	$1.36 \pm 0.17$	$1.22 \pm 0.10$	$1.15 \pm 0.08$	$1.95 \pm 0.64$
SL2SJ090408–005953	$1.27 \pm 0.31$	$1.29 \pm 0.16$	$1.08 \pm 0.10$	$0.98 \pm 0.07$	$0.61 \pm 0.20$
HSCJ090613+032939	$1.81 \pm 0.40$	$1.47 \pm 0.18$	$1.30 \pm 0.11$	$1.15 \pm 0.08$	$1.25 \pm 0.41$
H–ATLASJ090740.0–004200	$1.01 \pm 0.27$	$1.05 \pm 0.14$	$1.12 \pm 0.10$	$1.03 \pm 0.07$	$1.04 \pm 0.34$
SDSSJ0912+0029	$1.73 \pm 0.39$	$1.53 \pm 0.18$	$1.40 \pm 0.11$	$1.25 \pm 0.08$	$2.28 \pm 0.74$
SDSSJ0924+0219	$1.14 \pm 0.30$	$0.91 \pm 0.13$	$0.99 \pm 0.09$	$1.00 \pm 0.07$	$2.12 \pm 0.70$
SDSSJ0935–0003	$2.48 \pm 0.50$	$2.23 \pm 0.23$	$1.64 \pm 0.13$	$1.46 \pm 0.09$	$5.64 \pm 1.93$
BRI0952–0115	$0.41 \pm 0.17$	$0.75 \pm 0.12$	$0.80 \pm 0.08$	$0.88 \pm 0.06$	$0.77 \pm 0.25$
SDSSJ0955+0101	$1.21 \pm 0.31$	$1.10 \pm 0.15$	$0.93 \pm 0.09$	$0.99 \pm 0.07$	$1.23 \pm 0.40$
COSMOS5914+1219	$0.62 \pm 0.21$	$1.00 \pm 0.14$	$0.99 \pm 0.09$	$1.03 \pm 0.07$	$0.92 \pm 0.30$
COSMOS5921+0638	$0.98 \pm 0.28$	$1.10 \pm 0.15$	$1.06 \pm 0.10$	$1.06 \pm 0.07$	$0.74 \pm 0.24$
J095930.93+023427.7	$1.75 \pm 0.39$	$1.45 \pm 0.17$	$1.20 \pm 0.10$	$1.19 \pm 0.08$	$0.53 \pm 0.17$
COSMOS5939+3044	$1.81 \pm 0.39$	$1.89 \pm 0.21$	$1.79 \pm 0.13$	$1.68 \pm 0.10$	$5.77 \pm 2.05$
COSMOS0012+2015	$1.90 \pm 0.42$	$1.53 \pm 0.18$	$1.27 \pm 0.11$	$1.30 \pm 0.08$	$0.79 \pm 0.26$
COSMOS0018+3845	$1.37 \pm 0.33$	$1.60 \pm 0.18$	$1.46 \pm 0.12$	$1.38 \pm 0.09$	$1.39 \pm 0.46$
COSMOS0038+4133	$2.80 \pm 0.54$	$1.77 \pm 0.19$	$1.45 \pm 0.12$	$1.39 \pm 0.09$	$1.61 \pm 0.53$
COSMOS0047+5023	$1.44 \pm 0.35$	$0.95 \pm 0.13$	$1.09 \pm 0.10$	$1.09 \pm 0.07$	$4.62 \pm 1.60$
COSMOS0049+5128	$0.80 \pm 0.24$	$0.91 \pm 0.13$	$1.04 \pm 0.10$	$1.05 \pm 0.07$	$0.62 \pm 0.20$
COSMOS0050+4901	$1.81 \pm 0.38$	$1.50 \pm 0.18$	$1.27 \pm 0.11$	$1.19 \pm 0.08$	$5.01 \pm 1.73$
J100140.12+020040.9	$2.14 \pm 0.44$	$1.55 \pm 0.18$	$1.32 \pm 0.11$	$1.27 \pm 0.08$	$1.65 \pm 0.54$
SL2SJ100148+022207	$2.07 \pm 0.44$	$1.48 \pm 0.18$	$1.26 \pm 0.11$	$1.22 \pm 0.08$	$1.78 \pm 0.59$
COSMOS0211+1139	$1.97 \pm 0.42$	$1.61 \pm 0.19$	$1.63 \pm 0.13$	$1.36 \pm 0.08$	$5.04 \pm 1.74$
SL2SJ100212+022955	$1.24 \pm 0.31$	$1.35 \pm 0.17$	$1.28 \pm 0.11$	$1.24 \pm 0.08$	$1.35 \pm 0.45$
SL2SJ100215+023736	$1.10 \pm 0.29$	$1.21 \pm 0.15$	$1.23 \pm 0.10$	$1.27 \pm 0.08$	$1.08 \pm 0.35$
COSMOS0254+1430	$1.38 \pm 0.34$	$1.08 \pm 0.14$	$0.98 \pm 0.09$	$0.92 \pm 0.07$	$0.45 \pm 0.15$
SDSSJ1143–0144	$1.04 \pm 0.28$	$1.24 \pm 0.16$	$1.08 \pm 0.10$	$1.09 \pm 0.07$	$3.34 \pm 1.09$
HSTJ114331.46–014508.0	$1.02 \pm 0.28$	$1.02 \pm 0.14$	$1.08 \pm 0.10$	$1.05 \pm 0.07$	$3.51 \pm 1.15$
SDSSJ1159–0007	$2.00 \pm 0.43$	$1.45 \pm 0.17$	$1.14 \pm 0.10$	$1.18 \pm 0.08$	$2.24 \pm 0.74$
SDSSJ1215+0047	$1.55 \pm 0.36$	$1.23 \pm 0.16$	$1.15 \pm 0.10$	$1.12 \pm 0.08$	$2.00 \pm 0.67$
SDSSJ1226–0006	$1.19 \pm 0.31$	$1.08 \pm 0.15$	$1.23 \pm 0.11$	$1.19 \pm 0.08$	$0.43 \pm 0.14$
SDSSJ1250–0135	$1.43 \pm 0.35$	$1.14 \pm 0.15$	$1.29 \pm 0.11$	$1.34 \pm 0.08$	$0.49 \pm 0.16$
SDSSJ1347–0101	$1.06 \pm 0.28$	$0.88 \pm 0.13$	$0.97 \pm 0.09$	$0.98 \pm 0.07$	$0.54 \pm 0.18$
SDSSJ1403+0006	$1.96 \pm 0.42$	$1.47 \pm 0.18$	$1.38 \pm 0.11$	$1.25 \pm 0.08$	$2.12 \pm 0.69$
HSCJ141635+010128	$2.09 \pm 0.45$	$1.63 \pm 0.19$	$1.44 \pm 0.12$	$1.26 \pm 0.08$	$3.68 \pm 1.27$
HSCJ142053+005620	$1.50 \pm 0.36$	$1.28 \pm 0.16$	$1.28 \pm 0.11$	$1.23 \pm 0.08$	$2.34 \pm 0.78$
SDSSJ1436–0000	$1.46 \pm 0.34$	$1.14 \pm 0.15$	$0.99 \pm 0.09$	$1.07 \pm 0.07$	$1.47 \pm 0.47$
SDSSJ1524+4409	$1.15 \pm 0.30$	$1.45 \pm 0.17$	$1.37 \pm 0.11$	$1.24 \pm 0.08$	$1.60 \pm 0.52$
HSCJ155319+431824	$1.27 \pm 0.32$	$1.17 \pm 0.15$	$1.16 \pm 0.10$	$1.10 \pm 0.07$	$1.95 \pm 0.65$
B1600+434	$0.91 \pm 0.26$	$1.01 \pm 0.14$	$1.07 \pm 0.10$	$0.97 \pm 0.07$	$0.51 \pm 0.16$
SL2SJ220629+005728	$0.92 \pm 0.27$	$1.02 \pm 0.14$	$0.91 \pm 0.09$	$0.93 \pm 0.07$	$0.58 \pm 0.19$
SL2SJ221326–000946	$2.35 \pm 0.48$	$1.64 \pm 0.19$	$1.41 \pm 0.11$	$1.27 \pm 0.08$	$7.47 \pm 2.59$
SL2SJ221929–001743	$1.80 \pm 0.40$	$1.24 \pm 0.16$	$1.11 \pm 0.10$	$1.10 \pm 0.07$	$0.78 \pm 0.25$
SL2SJ222148+011542	$1.47 \pm 0.35$	$1.46 \pm 0.18$	$1.31 \pm 0.11$	$1.10 \pm 0.07$	$1.44 \pm 0.47$
SL2SJ222217+001202	$1.09 \pm 0.29$	$1.02 \pm 0.14$	$1.00 \pm 0.09$	$0.90 \pm 0.07$	$1.42 \pm 0.46$
Q2237+0305	$1.35 \pm 0.33$	$1.05 \pm 0.14$	$0.99 \pm 0.09$	$0.90 \pm 0.07$	$0.76 \pm 0.24$
SDSSJ2300+0022	$2.10 \pm 0.43$	$2.05 \pm 0.22$	$1.66 \pm 0.13$	$1.40 \pm 0.09$	$2.91 \pm 0.95$
HSCJ233230+003821	$1.25 \pm 0.31$	$1.18 \pm 0.15$	$1.19 \pm 0.10$	$1.13 \pm 0.08$	$1.31 \pm 0.43$

**Note.** Lenses listed here either do not have velocity dispersion measurements from BOSS or have unreliable velocity dispersion measurements, so they are not included in our main analysis. We list their local and LOS overdensities here for completeness.

## Appendix B

### Results Without Including Poisson Error on Number Counts

Tables 4 and 7 present the LOS and local overdensities of individual lens systems and their associated uncertainties. Those uncertainties are very conservative since we include Poisson error

on the raw counts,  $N$ , which are the main contributor to the error budget. However, there may be certain applications of these overdensities where greater precision is desired, so we reproduce those values with uncertainties that do not include Poisson error on  $N$  in Tables 8 and 9. We still account for Poisson error in  $N_{\text{rand}}$  and the error on the mean of the control sample.

**Table 8**  
Local and LOS Overdensity of Individual Lens Fields (No Poisson Error)

Lens	$N_{\text{eff}} / \langle N_{\text{eff}}^{\text{cont}} \rangle$ ( $r \leq 30''$ )	$N_{\text{eff}} / \langle N_{\text{eff}}^{\text{cont}} \rangle$ ( $r \leq 60''$ )	$N_{\text{eff}} / \langle N_{\text{eff}}^{\text{cont}} \rangle$ ( $r \leq 90''$ )	$N_{\text{eff}} / \langle N_{\text{eff}}^{\text{cont}} \rangle$ ( $r \leq 120''$ )	$\Sigma_{10} / \langle \Sigma_{10}^{\text{cont}} \rangle$
HSCJ015731–033057	1.33 ± 0.16	1.48 ± 0.09	1.45 ± 0.06	1.26 ± 0.04	2.37 ± 0.27
HSCJ015756–021809	1.68 ± 0.21	1.10 ± 0.07	1.02 ± 0.04	0.95 ± 0.03	0.87 ± 0.07
SDSSJ0157–0056	0.75 ± 0.09	1.00 ± 0.06	1.12 ± 0.05	1.20 ± 0.04	1.32 ± 0.11
HSCJ020141–030946	1.54 ± 0.19	1.15 ± 0.07	0.96 ± 0.04	1.02 ± 0.03	2.61 ± 0.26
HSCJ020241–064611	1.28 ± 0.15	0.95 ± 0.06	1.03 ± 0.05	1.13 ± 0.04	1.05 ± 0.08
HSCJ020846–032727	1.71 ± 0.20	1.36 ± 0.08	1.30 ± 0.06	1.33 ± 0.04	3.42 ± 0.44
SL2SJ021737–051329	1.90 ± 0.22	1.53 ± 0.10	1.19 ± 0.05	1.10 ± 0.04	4.49 ± 0.63
HSCJ022140–021020	1.26 ± 0.14	0.82 ± 0.05	0.86 ± 0.04	0.86 ± 0.03	5.02 ± 0.75
SL2SJ022315–062906	1.90 ± 0.25	1.16 ± 0.07	1.01 ± 0.04	0.91 ± 0.03	4.24 ± 0.55
SL2SJ022346–053418	1.80 ± 0.22	1.16 ± 0.07	1.06 ± 0.05	1.09 ± 0.04	2.21 ± 0.22
SL2SJ022357–065142	1.29 ± 0.14	0.98 ± 0.06	1.05 ± 0.04	1.04 ± 0.03	1.37 ± 0.11
SL2SJ022439–040045	1.35 ± 0.18	0.87 ± 0.05	0.96 ± 0.04	1.05 ± 0.03	2.06 ± 0.20
SL2SJ022511–045433	1.40 ± 0.16	1.20 ± 0.07	1.15 ± 0.05	1.10 ± 0.04	1.05 ± 0.06
SL2SJ022610–042011	1.56 ± 0.17	0.93 ± 0.06	0.91 ± 0.04	0.97 ± 0.03	1.13 ± 0.09
HSCJ023217–021703	1.21 ± 0.14	1.14 ± 0.07	1.15 ± 0.05	1.02 ± 0.03	1.11 ± 0.09
SL2SJ023307–043838	1.41 ± 0.17	1.22 ± 0.08	1.19 ± 0.05	1.11 ± 0.04	1.33 ± 0.13
HSCJ023538–063406	1.57 ± 0.18	1.06 ± 0.06	0.93 ± 0.04	0.87 ± 0.03	1.05 ± 0.07
HSCJ023637–033220	1.86 ± 0.22	1.57 ± 0.10	1.49 ± 0.06	1.36 ± 0.04	4.08 ± 0.39
HSCJ023655–023656	1.04 ± 0.13	0.97 ± 0.06	0.94 ± 0.04	0.97 ± 0.03	2.03 ± 0.20
HSCJ083943+004740	1.05 ± 0.13	1.03 ± 0.06	1.01 ± 0.04	1.10 ± 0.04	1.48 ± 0.14
HSCJ085855–010208	2.35 ± 0.29	1.22 ± 0.08	1.16 ± 0.05	1.01 ± 0.03	1.20 ± 0.10
HSCJ090507–001030	1.26 ± 0.15	0.96 ± 0.06	0.89 ± 0.04	0.93 ± 0.03	1.48 ± 0.13
HSCJ090709+005648	1.45 ± 0.17	0.92 ± 0.06	0.98 ± 0.04	0.99 ± 0.03	1.21 ± 0.10
SDSSJ0915–0055	2.61 ± 0.35	1.96 ± 0.13	1.52 ± 0.07	1.38 ± 0.05	3.22 ± 0.36
HSCJ091608+034710	1.13 ± 0.15	1.21 ± 0.08	1.09 ± 0.05	1.06 ± 0.04	3.57 ± 0.43
HSCJ091904+033638	1.47 ± 0.17	1.24 ± 0.08	1.09 ± 0.05	1.01 ± 0.03	4.57 ± 0.57
HSCJ092101+035521	1.59 ± 0.20	1.00 ± 0.06	0.83 ± 0.04	0.81 ± 0.03	1.64 ± 0.14
HSCJ093506–020031	1.42 ± 0.18	0.85 ± 0.06	0.72 ± 0.03	0.76 ± 0.03	1.21 ± 0.10
HSCJ094123+000446	1.32 ± 0.16	1.00 ± 0.06	0.94 ± 0.04	0.88 ± 0.03	1.80 ± 0.17
SDSSJ0944–0147	1.79 ± 0.22	1.64 ± 0.10	1.30 ± 0.06	1.12 ± 0.04	2.01 ± 0.19
HSCJ095750+014507	0.97 ± 0.12	0.86 ± 0.05	0.87 ± 0.04	0.91 ± 0.03	1.10 ± 0.09
COSMOS0013+2249	0.93 ± 0.11	1.09 ± 0.07	1.12 ± 0.05	1.15 ± 0.04	4.10 ± 0.48
COSMOS0056+1226	1.12 ± 0.12	0.99 ± 0.06	1.00 ± 0.04	0.99 ± 0.03	2.16 ± 0.20
HSCJ100659+024735	1.95 ± 0.24	1.28 ± 0.08	1.11 ± 0.05	1.00 ± 0.03	7.93 ± 1.32
HSCJ114311–013935	0.92 ± 0.11	0.96 ± 0.06	1.07 ± 0.05	1.14 ± 0.04	1.47 ± 0.14
HSCJ115653–003948	1.19 ± 0.14	1.36 ± 0.08	1.38 ± 0.06	1.43 ± 0.05	1.18 ± 0.09
HSCJ120623+001507	1.41 ± 0.17	1.13 ± 0.07	1.14 ± 0.05	1.22 ± 0.04	3.66 ± 0.45
HSCJ121052–011905	0.85 ± 0.11	1.06 ± 0.07	1.03 ± 0.04	1.19 ± 0.04	1.49 ± 0.15
HSCJ122048+002145	3.11 ± 0.38	2.06 ± 0.13	1.62 ± 0.07	1.52 ± 0.05	5.71 ± 0.78
HSCJ122314–002939	1.25 ± 0.18	1.32 ± 0.09	1.19 ± 0.05	1.07 ± 0.04	1.66 ± 0.15
HSCJ123825+003212	2.00 ± 0.25	1.37 ± 0.08	1.26 ± 0.05	1.18 ± 0.04	2.56 ± 0.27
HSCJ124320–004517	2.10 ± 0.27	1.40 ± 0.09	1.27 ± 0.05	1.14 ± 0.04	4.09 ± 0.56
HSCJ125254+004356	1.57 ± 0.19	1.43 ± 0.09	1.25 ± 0.05	1.08 ± 0.04	2.43 ± 0.28
HSCJ134351+010817	1.67 ± 0.20	1.51 ± 0.10	1.33 ± 0.06	1.18 ± 0.04	2.76 ± 0.31
HSCJ135038+002550	1.49 ± 0.19	1.40 ± 0.09	1.19 ± 0.05	1.03 ± 0.03	2.32 ± 0.24
HSCJ135138+002839	2.71 ± 0.35	1.46 ± 0.09	1.46 ± 0.06	1.35 ± 0.05	8.16 ± 1.37
HSCJ135242–002614	0.70 ± 0.08	0.77 ± 0.05	0.84 ± 0.04	0.93 ± 0.03	0.75 ± 0.05
HSCJ135853–021525	2.03 ± 0.26	1.37 ± 0.09	1.21 ± 0.05	1.22 ± 0.04	3.60 ± 0.47
HSCJ140929–011410	1.36 ± 0.16	1.66 ± 0.10	1.34 ± 0.06	1.27 ± 0.04	2.28 ± 0.23
HSCJ141001+012956	1.19 ± 0.14	1.12 ± 0.07	1.09 ± 0.05	1.17 ± 0.04	1.82 ± 0.17
HSCJ141300–012608	1.10 ± 0.13	0.93 ± 0.06	0.92 ± 0.04	0.97 ± 0.03	0.74 ± 0.06
HSCJ141831–000052	1.63 ± 0.19	1.59 ± 0.10	1.15 ± 0.05	1.15 ± 0.04	2.44 ± 0.20
HSCJ142353+013446	1.30 ± 0.15	1.31 ± 0.08	1.08 ± 0.05	1.11 ± 0.04	2.19 ± 0.22

**Table 8**  
(Continued)

Lens	$N_{\text{eff}} / \langle N_{\text{eff}}^{\text{cont}} \rangle$ ( $r \leq 30''$ )	$N_{\text{eff}} / \langle N_{\text{eff}}^{\text{cont}} \rangle$ ( $r \leq 60''$ )	$N_{\text{eff}} / \langle N_{\text{eff}}^{\text{cont}} \rangle$ ( $r \leq 90''$ )	$N_{\text{eff}} / \langle N_{\text{eff}}^{\text{cont}} \rangle$ ( $r \leq 120''$ )	$\Sigma_{10} / \langle \Sigma_{10}^{\text{cont}} \rangle$
HSCJ142449–005321	$3.20 \pm 0.42$	$1.79 \pm 0.11$	$1.74 \pm 0.08$	$1.68 \pm 0.06$	$8.54 \pm 1.64$
HSCJ142720+001916	$1.55 \pm 0.18$	$1.49 \pm 0.09$	$1.38 \pm 0.06$	$1.31 \pm 0.04$	$3.21 \pm 0.37$
HSCJ142748+000958	$1.30 \pm 0.15$	$1.36 \pm 0.09$	$1.17 \pm 0.05$	$1.27 \pm 0.04$	$2.05 \pm 0.20$
HSCJ144307–004056	$0.76 \pm 0.10$	$1.06 \pm 0.07$	$0.99 \pm 0.04$	$0.96 \pm 0.03$	$1.34 \pm 0.11$
HSCJ144428–005142	$1.96 \pm 0.24$	$1.26 \pm 0.08$	$1.09 \pm 0.05$	$1.09 \pm 0.04$	$8.53 \pm 1.53$
HSCJ145236–002142	$2.63 \pm 0.33$	$1.61 \pm 0.10$	$1.35 \pm 0.06$	$1.18 \pm 0.04$	$6.60 \pm 1.13$
HSCJ145732–015917	$2.61 \pm 0.34$	$1.48 \pm 0.09$	$1.34 \pm 0.06$	$1.16 \pm 0.04$	$4.93 \pm 0.69$
HSCJ145759+423019	$1.56 \pm 0.17$	$1.10 \pm 0.07$	$1.13 \pm 0.05$	$1.11 \pm 0.04$	$4.11 \pm 0.57$
HSCJ145902–012351	$1.00 \pm 0.11$	$1.01 \pm 0.06$	$0.88 \pm 0.04$	$1.00 \pm 0.03$	$1.38 \pm 0.12$
HSCJ151336+433251	$1.12 \pm 0.13$	$1.40 \pm 0.09$	$1.21 \pm 0.05$	$1.13 \pm 0.04$	$2.63 \pm 0.28$
HSCJ155826+432830	$1.35 \pm 0.17$	$1.07 \pm 0.07$	$0.93 \pm 0.04$	$1.02 \pm 0.03$	$1.04 \pm 0.08$
SL2SJ220202+014710	$0.78 \pm 0.10$	$0.67 \pm 0.04$	$0.84 \pm 0.04$	$0.88 \pm 0.03$	$0.86 \pm 0.06$
SL2SJ220506+014703	$2.22 \pm 0.29$	$1.69 \pm 0.12$	$1.45 \pm 0.07$	$1.35 \pm 0.05$	$1.83 \pm 0.16$
HSCJ220550+041524	$1.81 \pm 0.22$	$1.38 \pm 0.09$	$1.27 \pm 0.06$	$1.20 \pm 0.04$	$2.07 \pm 0.16$
SL2SJ220642+041131	$1.79 \pm 0.22$	$1.34 \pm 0.08$	$1.07 \pm 0.05$	$1.00 \pm 0.03$	$5.17 \pm 0.79$
HSCJ221726+000350	$1.16 \pm 0.14$	$1.09 \pm 0.07$	$1.01 \pm 0.04$	$0.91 \pm 0.03$	$7.10 \pm 1.05$
SL2SJ221852+014038	$1.06 \pm 0.13$	$1.04 \pm 0.06$	$0.93 \pm 0.04$	$1.00 \pm 0.03$	$1.62 \pm 0.15$
HSCJ222801+012805	$1.10 \pm 0.13$	$1.00 \pm 0.06$	$1.02 \pm 0.04$	$1.11 \pm 0.04$	$1.36 \pm 0.13$
HSCJ223518–004747	$1.16 \pm 0.13$	$1.14 \pm 0.07$	$1.13 \pm 0.05$	$1.09 \pm 0.04$	$4.38 \pm 0.62$
HSCJ223733+005015	$0.83 \pm 0.10$	$1.06 \pm 0.07$	$0.95 \pm 0.04$	$0.96 \pm 0.03$	$1.33 \pm 0.12$
HSCJ224201+022810	$1.51 \pm 0.19$	$0.98 \pm 0.06$	$0.90 \pm 0.04$	$1.05 \pm 0.03$	$1.28 \pm 0.10$
HSCJ224221+001144	$1.14 \pm 0.14$	$0.95 \pm 0.06$	$1.21 \pm 0.05$	$1.18 \pm 0.04$	$2.81 \pm 0.29$
HSCJ224454+031551	$1.29 \pm 0.15$	$1.11 \pm 0.07$	$1.01 \pm 0.04$	$1.03 \pm 0.03$	$1.39 \pm 0.13$
HSCJ224800–010259	$1.34 \pm 0.16$	$1.19 \pm 0.07$	$1.22 \pm 0.05$	$1.04 \pm 0.04$	$1.64 \pm 0.12$
HSCJ225800+004533	$1.02 \pm 0.12$	$1.30 \pm 0.08$	$1.19 \pm 0.05$	$1.14 \pm 0.04$	$1.93 \pm 0.19$
SDSSJ2303+0037	$1.96 \pm 0.25$	$1.30 \pm 0.09$	$1.16 \pm 0.05$	$1.11 \pm 0.04$	$3.17 \pm 0.36$
HSCJ230521–000211	$1.59 \pm 0.18$	$1.08 \pm 0.07$	$0.89 \pm 0.04$	$0.87 \pm 0.03$	$1.42 \pm 0.12$
HSCJ231004+024759	$3.30 \pm 0.43$	$2.00 \pm 0.13$	$1.71 \pm 0.08$	$1.50 \pm 0.05$	$10.29 \pm 1.71$
HSCJ231145–013039	$1.61 \pm 0.18$	$1.14 \pm 0.07$	$1.02 \pm 0.04$	$1.02 \pm 0.03$	$1.99 \pm 0.20$
HSCJ232415+011331	$1.04 \pm 0.13$	$0.95 \pm 0.06$	$1.02 \pm 0.04$	$1.16 \pm 0.04$	$1.80 \pm 0.17$
HSCJ233130+003733	$1.39 \pm 0.16$	$1.14 \pm 0.07$	$1.33 \pm 0.06$	$1.39 \pm 0.05$	$1.41 \pm 0.12$
HSCJ233146+013845	$1.44 \pm 0.17$	$1.15 \pm 0.07$	$1.11 \pm 0.05$	$1.05 \pm 0.04$	$3.48 \pm 0.39$
HSCJ233311+022310	$1.06 \pm 0.12$	$0.91 \pm 0.06$	$0.98 \pm 0.04$	$0.89 \pm 0.03$	$1.07 \pm 0.08$
HSCJ233528+001355	$1.75 \pm 0.20$	$1.32 \pm 0.08$	$1.15 \pm 0.05$	$1.24 \pm 0.04$	$4.01 \pm 0.51$

**Note.** Relative LOS overdensities are calculated for a magnitude limit of  $i \leq 24$ . Overdensities are normalized by the mean values across all control fields. The uncertainties do not include Poisson uncertainties in the calculation of lens field quantities.

**Table 9**  
Local and LOS Overdensity of Individual Lens Fields Not in Main Sample (No Poisson Error)

Lens	$N_{\text{eff}} / \langle N_{\text{eff}}^{\text{cont}} \rangle$ ( $r \leq 30''$ )	$N_{\text{eff}} / \langle N_{\text{eff}}^{\text{cont}} \rangle$ ( $r \leq 60''$ )	$N_{\text{eff}} / \langle N_{\text{eff}}^{\text{cont}} \rangle$ ( $r \leq 90''$ )	$N_{\text{eff}} / \langle N_{\text{eff}}^{\text{cont}} \rangle$ ( $r \leq 120''$ )	$\Sigma_{10} / \langle \Sigma_{10}^{\text{cont}} \rangle$
SL2SJ021247–055552	$1.30 \pm 0.16$	$0.95 \pm 0.06$	$1.11 \pm 0.05$	$1.25 \pm 0.04$	$2.74 \pm 0.32$
SL2SJ021411–040502	$1.85 \pm 0.24$	$1.34 \pm 0.09$	$1.20 \pm 0.05$	$1.13 \pm 0.04$	$4.18 \pm 0.58$
SL2SJ022056–063934	$0.30 \pm 0.04$	$0.73 \pm 0.05$	$0.77 \pm 0.03$	$0.88 \pm 0.03$	$0.68 \pm 0.05$
SL2SJ022459–040104	$0.84 \pm 0.10$	$0.97 \pm 0.06$	$0.98 \pm 0.04$	$0.94 \pm 0.03$	$0.78 \pm 0.06$
SL2SJ022648–040610	$1.40 \pm 0.16$	$0.97 \pm 0.06$	$0.94 \pm 0.04$	$1.05 \pm 0.04$	$1.94 \pm 0.21$
SL2SJ023251–040823	$1.80 \pm 0.23$	$1.08 \pm 0.07$	$1.03 \pm 0.04$	$1.05 \pm 0.04$	$1.58 \pm 0.14$
SDSSJ023740.63–064112.9	$0.77 \pm 0.09$	$0.75 \pm 0.05$	$0.85 \pm 0.04$	$0.82 \pm 0.03$	$0.95 \pm 0.07$
SL2SJ085540–014730	$1.30 \pm 0.15$	$1.17 \pm 0.07$	$1.25 \pm 0.05$	$1.02 \pm 0.03$	$1.34 \pm 0.11$
SL2SJ085826–014300	$1.35 \pm 0.16$	$1.36 \pm 0.09$	$1.22 \pm 0.05$	$1.15 \pm 0.04$	$1.95 \pm 0.19$
SL2SJ090408–005953	$1.27 \pm 0.14$	$1.29 \pm 0.08$	$1.08 \pm 0.05$	$0.98 \pm 0.03$	$0.61 \pm 0.05$
HSCJ090613+032939	$1.81 \pm 0.21$	$1.47 \pm 0.09$	$1.30 \pm 0.06$	$1.15 \pm 0.04$	$1.25 \pm 0.11$
H-ATLASJ090740.0–004200	$1.01 \pm 0.11$	$1.05 \pm 0.06$	$1.12 \pm 0.05$	$1.03 \pm 0.03$	$1.04 \pm 0.09$
SDSSJ0912+0029	$1.73 \pm 0.22$	$1.53 \pm 0.10$	$1.40 \pm 0.06$	$1.25 \pm 0.04$	$2.28 \pm 0.18$
SDSSJ0924+0219	$1.14 \pm 0.13$	$0.91 \pm 0.05$	$0.99 \pm 0.04$	$1.00 \pm 0.03$	$2.12 \pm 0.21$
SDSSJ0935–0003	$2.48 \pm 0.31$	$2.23 \pm 0.14$	$1.64 \pm 0.07$	$1.46 \pm 0.05$	$5.64 \pm 0.73$
BRI0952–0115	$0.41 \pm 0.05$	$0.75 \pm 0.05$	$0.80 \pm 0.03$	$0.88 \pm 0.03$	$0.77 \pm 0.06$
SDSSJ0955+0101	$1.21 \pm 0.14$	$1.10 \pm 0.07$	$0.93 \pm 0.04$	$0.99 \pm 0.03$	$1.23 \pm 0.09$
COSMOS5914+1219	$0.62 \pm 0.07$	$1.00 \pm 0.06$	$0.99 \pm 0.04$	$1.03 \pm 0.03$	$0.92 \pm 0.06$
COSMOS5921+0638	$0.98 \pm 0.13$	$1.10 \pm 0.07$	$1.06 \pm 0.05$	$1.06 \pm 0.04$	$0.74 \pm 0.05$
J095930.93+023427.7	$1.75 \pm 0.21$	$1.45 \pm 0.09$	$1.20 \pm 0.05$	$1.19 \pm 0.04$	$0.53 \pm 0.03$
COSMOS5939+3044	$1.81 \pm 0.20$	$1.89 \pm 0.12$	$1.79 \pm 0.08$	$1.68 \pm 0.06$	$5.77 \pm 0.93$
COSMOS0012+2015	$1.90 \pm 0.25$	$1.53 \pm 0.10$	$1.27 \pm 0.06$	$1.30 \pm 0.04$	$0.79 \pm 0.06$
COSMOS0018+3845	$1.37 \pm 0.15$	$1.60 \pm 0.10$	$1.46 \pm 0.06$	$1.38 \pm 0.05$	$1.39 \pm 0.12$
COSMOS0038+4133	$2.80 \pm 0.34$	$1.77 \pm 0.11$	$1.45 \pm 0.06$	$1.39 \pm 0.05$	$1.61 \pm 0.16$
COSMOS0047+5023	$1.44 \pm 0.18$	$0.95 \pm 0.06$	$1.09 \pm 0.05$	$1.09 \pm 0.04$	$4.62 \pm 0.64$
COSMOS0049+5128	$0.80 \pm 0.09$	$0.91 \pm 0.06$	$1.04 \pm 0.05$	$1.05 \pm 0.04$	$0.62 \pm 0.04$
COSMOS0050+4901	$1.81 \pm 0.19$	$1.50 \pm 0.09$	$1.27 \pm 0.06$	$1.19 \pm 0.04$	$5.01 \pm 0.69$
J100140.12+020040.9	$2.14 \pm 0.25$	$1.55 \pm 0.10$	$1.32 \pm 0.06$	$1.27 \pm 0.04$	$1.65 \pm 0.15$
SL2SJ100148+022207	$2.07 \pm 0.25$	$1.48 \pm 0.09$	$1.26 \pm 0.06$	$1.22 \pm 0.04$	$1.78 \pm 0.19$
COSMOS0211+1139	$1.97 \pm 0.24$	$1.61 \pm 0.10$	$1.63 \pm 0.07$	$1.36 \pm 0.05$	$5.04 \pm 0.69$
SL2SJ100212+022955	$1.24 \pm 0.13$	$1.35 \pm 0.09$	$1.28 \pm 0.06$	$1.24 \pm 0.04$	$1.35 \pm 0.13$
SL2SJ100215+023736	$1.10 \pm 0.12$	$1.21 \pm 0.07$	$1.23 \pm 0.05$	$1.27 \pm 0.04$	$1.08 \pm 0.09$
COSMOS0254+1430	$1.38 \pm 0.17$	$1.08 \pm 0.07$	$0.98 \pm 0.04$	$0.92 \pm 0.03$	$0.45 \pm 0.03$
SDSSJ1143–0144	$1.04 \pm 0.12$	$1.24 \pm 0.08$	$1.08 \pm 0.05$	$1.09 \pm 0.04$	$3.34 \pm 0.28$
HSTJ114331.46–014508.0	$1.02 \pm 0.12$	$1.02 \pm 0.07$	$1.08 \pm 0.05$	$1.05 \pm 0.04$	$3.51 \pm 0.29$
SDSSJ1159–0007	$2.00 \pm 0.24$	$1.45 \pm 0.09$	$1.14 \pm 0.05$	$1.18 \pm 0.04$	$2.24 \pm 0.23$
SDSSJ1215+0047	$1.55 \pm 0.19$	$1.23 \pm 0.08$	$1.15 \pm 0.05$	$1.12 \pm 0.04$	$2.00 \pm 0.21$
SDSSJ1226–0006	$1.19 \pm 0.15$	$1.08 \pm 0.07$	$1.23 \pm 0.06$	$1.19 \pm 0.04$	$0.43 \pm 0.03$
SDSSJ1250–0135	$1.43 \pm 0.18$	$1.14 \pm 0.07$	$1.29 \pm 0.06$	$1.34 \pm 0.04$	$0.49 \pm 0.04$
SDSSJ1347–0101	$1.06 \pm 0.11$	$0.88 \pm 0.05$	$0.97 \pm 0.04$	$0.98 \pm 0.03$	$0.54 \pm 0.04$
SDSSJ1403+0006	$1.96 \pm 0.23$	$1.47 \pm 0.09$	$1.38 \pm 0.06$	$1.25 \pm 0.04$	$2.12 \pm 0.15$
HSCJ141635+010128	$2.09 \pm 0.27$	$1.63 \pm 0.10$	$1.44 \pm 0.06$	$1.26 \pm 0.04$	$3.68 \pm 0.50$
HSCJ142053+005620	$1.50 \pm 0.18$	$1.28 \pm 0.08$	$1.28 \pm 0.06$	$1.23 \pm 0.04$	$2.34 \pm 0.26$
SDSSJ1436–0000	$1.46 \pm 0.17$	$1.14 \pm 0.07$	$0.99 \pm 0.04$	$1.07 \pm 0.04$	$1.47 \pm 0.10$
SDSSJ1524+4409	$1.15 \pm 0.14$	$1.45 \pm 0.09$	$1.37 \pm 0.06$	$1.24 \pm 0.04$	$1.60 \pm 0.13$
HSCJ155319+431824	$1.27 \pm 0.15$	$1.17 \pm 0.07$	$1.16 \pm 0.05$	$1.10 \pm 0.04$	$1.95 \pm 0.20$
B1600+434	$0.91 \pm 0.10$	$1.01 \pm 0.07$	$1.07 \pm 0.05$	$0.97 \pm 0.03$	$0.51 \pm 0.04$
SL2SJ220629+005728	$0.92 \pm 0.12$	$1.02 \pm 0.07$	$0.91 \pm 0.04$	$0.93 \pm 0.03$	$0.58 \pm 0.04$
SL2SJ221326–000946	$2.35 \pm 0.29$	$1.64 \pm 0.11$	$1.41 \pm 0.06$	$1.27 \pm 0.04$	$7.47 \pm 1.06$
SL2SJ221929–001743	$1.80 \pm 0.23$	$1.24 \pm 0.08$	$1.11 \pm 0.05$	$1.10 \pm 0.04$	$0.78 \pm 0.05$
SL2SJ222148+011542	$1.47 \pm 0.17$	$1.46 \pm 0.09$	$1.31 \pm 0.06$	$1.10 \pm 0.04$	$1.44 \pm 0.12$
SL2SJ222217+001202	$1.09 \pm 0.13$	$1.02 \pm 0.06$	$1.00 \pm 0.04$	$0.90 \pm 0.03$	$1.42 \pm 0.12$
Q2237+0305	$1.35 \pm 0.16$	$1.05 \pm 0.07$	$0.99 \pm 0.04$	$0.90 \pm 0.03$	$0.76 \pm 0.04$
SDSSJ2300+0022	$2.10 \pm 0.24$	$2.05 \pm 0.13$	$1.66 \pm 0.07$	$1.40 \pm 0.05$	$2.91 \pm 0.23$
HSCJ233230+003821	$1.25 \pm 0.14$	$1.18 \pm 0.07$	$1.19 \pm 0.05$	$1.13 \pm 0.04$	$1.31 \pm 0.12$

**Note.** Lenses listed here either do not have velocity dispersion measurements from BOSS or have unreliable velocity dispersion measurements, so they are not included in our main analysis. We list their local and LOS overdensities here for completeness. The uncertainties do not include Poisson uncertainties in the calculation of lens field quantites.

## ORCID iDs

- Kenneth C. Wong [DOI](https://orcid.org/0000-0002-8459-7793)  
 James H. H. Chan [DOI](https://orcid.org/0000-0001-8797-725X)  
 Masayuki Tanaka [DOI](https://orcid.org/0000-0002-5011-5178)  
 Anupreeta More [DOI](https://orcid.org/0000-0001-7714-7076)  
 Masamune Oguri [DOI](https://orcid.org/0000-0003-3484-399X)

## References

- Abazajian, K., Adelman-McCarthy, J. K., Agüeros, M. A., et al. 2004, *AJ*, **128**, 502  
 Abolfathi, B., Aguado, D. S., Aguilar, G., et al. 2018, *ApJS*, **235**, 42  
 Aihara, H., Arimoto, N., Armstrong, R., et al. 2018a, *PASJ*, **70**, S4  
 Aihara, H., Armstrong, R., Bickerton, S., et al. 2018b, *PASJ*, **70**, S8  
 Alam, S., Albareti, F. D., Allende Prieto, C., et al. 2015, *ApJS*, **219**, 12  
 Auger, M. W., Treu, T., Bolton, A. S., et al. 2010, *ApJ*, **724**, 511  
 Auger, M. W., Treu, T., Brewer, B. J., & Marshall, P. J. 2011, *MNRAS*, **411**, L6  
 Axelrod, T., Kantor, J., Lupton, R. H., & Pierfederici, F. 2010, *Proc. SPIE*, **7740**, 774015  
 Bolton, A. S., Burles, S., Koopmans, L. V. E., Treu, T., & Moustakas, L. A. 2006, *ApJ*, **638**, 703  
 Bolton, A. S., Treu, T., Koopmans, L. V. E., et al. 2008, *ApJ*, **684**, 248  
 Bonvin, V., Courbin, F., Suyu, S. H., et al. 2017, *MNRAS*, **465**, 4914  
 Bosch, J., Armstrong, R., Bickerton, S., et al. 2018, *PASJ*, **70**, S5  
 Brownstein, J. R., Bolton, A. S., Schlegel, D. J., et al. 2012, *ApJ*, **744**, 41  
 Chan, J. H. H., Suyu, S. H., Chiueh, T., et al. 2015, *ApJ*, **807**, 138  
 Chiu, I., Dietrich, J. P., Mohr, J., et al. 2016, *MNRAS*, **457**, 3050  
 Collett, T. E. 2015, *ApJ*, **811**, 20  
 Collett, T. E., & Cunningham, S. D. 2016, *MNRAS*, **462**, 3255  
 Collett, T. E., Marshall, P. J., Auger, M. W., et al. 2013, *MNRAS*, **432**, 679  
 Cooper, M. C., Newman, J. A., Croton, D. J., et al. 2006, *MNRAS*, **370**, 198  
 Cooper, M. C., Newman, J. A., Madgwick, D. S., et al. 2005, *ApJ*, **634**, 833  
 Coupon, J., Czakon, N., Bosch, J., et al. 2018, *PASJ*, **70**, S7  
 Dawson, K. S., Schlegel, D. J., Ahn, C. P., et al. 2013, *AJ*, **145**, 10  
 Dressler, A. 1980, *ApJ*, **236**, 351  
 Eigenbrod, A., Courbin, F., Dye, S., et al. 2006, *A&A*, **451**, 747  
 Eigenbrod, A., Courbin, F., & Meylan, G. 2007, *A&A*, **465**, 51  
 Eisenstein, D. J., Weinberg, D. H., Agol, E., et al. 2011, *AJ*, **142**, 72  
 Falco, E. E., Gorenstein, M. V., & Shapiro, I. I. 1985, *ApJL*, **289**, L1  
 Fassnacht, C. D., & Cohen, J. G. 1998, *AJ*, **115**, 377  
 Fassnacht, C. D., Koopmans, L. V. E., & Wong, K. C. 2011, *MNRAS*, **410**, 2167  
 Faure, C., Anguita, T., Alloin, D., et al. 2011, *A&A*, **529**, A72  
 Faure, C., Kneib, J.-P., Covone, G., et al. 2008, *ApJS*, **176**, 19  
 Freedman, W. L., Madore, B. F., Scowcroft, V., et al. 2012, *ApJ*, **758**, 24  
 Furusawa, H., Koike, M., Takata, T., et al. 2018, *PASJ*, **70**, S3  
 Gorenstein, M. V., Falco, E. E., & Shapiro, I. I. 1988, *ApJ*, **327**, 693  
 Greene, Z. S., Suyu, S. H., Treu, T., et al. 2013, *ApJ*, **768**, 39  
 Hilbert, S., White, S. D. M., Hartlap, J., & Schneider, P. 2007, *MNRAS*, **382**, 121  
 Huchra, J., Gorenstein, M., Kent, S., et al. 1985, *AJ*, **90**, 691  
 Inada, N., Becker, R. H., Burles, S., et al. 2003, *AJ*, **126**, 666  
 Inada, N., Oguri, M., Becker, R. H., et al. 2008, *AJ*, **135**, 496  
 Jackson, N., de Bruyn, A. G., Myers, S., et al. 1995, *MNRAS*, **274**, L25  
 Jurić, M., Kantor, J., Lim, K., et al. 2017, in ASP Conf. Ser. 512, Astronomical Data Analysis Software and Systems XXV, ed. N. P. F. Lorente et al. (San Francisco, CA: ASP), 279  
 Kawanomoto, S., Uraguchi, F., Komiyama, Y., et al. 2018, *PASJ*, **70**, 66  
 Keeton, C. R. 2001, arXiv:astro-ph/0102340  
 Kelly, B. C. 2007, *ApJ*, **665**, 1489  
 Komiyama, Y., Obuchi, Y., Nakaya, H., et al. 2018, *PASJ*, **70**, S2  
 Koopmans, L. V. E., Bolton, A., Treu, T., et al. 2009, *ApJL*, **703**, L51  
 McCully, C., Keeton, C. R., Wong, K. C., & Zabludoff, A. I. 2014, *MNRAS*, **443**, 3631  
 McCully, C., Keeton, C. R., Wong, K. C., & Zabludoff, A. I. 2017, *ApJ*, **836**, 141  
 McMahon, R., Irwin, M., & Hazard, C. 1992, *Gemin*, **36**, 1  
 Miyazaki, S., Komiyama, Y., Kawanomoto, S., et al. 2018, *PASJ*, **70**, S1  
 Miyazaki, S., Komiyama, Y., Nakaya, H., et al. 2012, *Proc. SPIE*, **8446**, 84460Z  
 Momcheva, I., Williams, K., Keeton, C., & Zabludoff, A. 2006, *ApJ*, **641**, 169  
 More, A., Cabanac, R., More, S., et al. 2012, *ApJ*, **749**, 38  
 Navarro, J. F., Frenk, C. S., & White, S. D. M. 1997, *ApJ*, **490**, 493  
 Negrello, M., Hopwood, R., De Zotti, G., et al. 2010, *Sci*, **330**, 800  
 Newton, E. R., Marshall, P. J., & Treu, T. 2009, *ApJ*, **696**, 1125  
 Oguri, M., Inada, N., Clocchiatti, A., et al. 2008, *AJ*, **135**, 520  
 Oguri, M., Keeton, C. R., & Dadal, N. 2005, *MNRAS*, **364**, 1451  
 Refsdal, S. 1964, *MNRAS*, **128**, 307  
 Riess, A. G., Macri, L. M., Hoffmann, S. L., et al. 2016, *ApJ*, **826**, 56  
 Rusu, C. E., Fassnacht, C. D., Sluse, D., et al. 2017, *MNRAS*, **467**, 4220  
 Saha, P. 2000, *AJ*, **120**, 1654  
 Schneider, P., & Sluse, D. 2013, *A&A*, **559**, A37  
 Shu, Y., Bolton, A. S., Kochanek, C. S., et al. 2016, *ApJ*, **824**, 86  
 Sluse, D., Sonnenfeld, A., Rumbaugh, N., et al. 2017, *MNRAS*, **470**, 4838  
 Sonnenfeld, A., Chan, J. H. H., Shu, Y., et al. 2018, *PASJ*, **70**, S29  
 Sonnenfeld, A., Gavazzi, R., Suyu, S. H., Treu, T., & Marshall, P. J. 2013a, *ApJ*, **777**, 97  
 Sonnenfeld, A., Treu, T., Gavazzi, R., et al. 2013b, *ApJ*, **777**, 98  
 Sonnenfeld, A., Chan, J. H. H., Treu, T., et al. 2017, *MNRAS*, **468**, 2590  
 Tanaka, M. 2015, *ApJ*, **801**, 20  
 Tanaka, M., Coupon, J., Hsieh, B.-C., et al. 2018, *PASJ*, **70**, S9  
 Tanaka, M., Wong, K. C., More, A., et al. 2016, *ApJL*, **826**, L19  
 Treu, T., Gavazzi, R., Gorecki, A., et al. 2009, *ApJ*, **690**, 670  
 Treu, T., Koopmans, L. V., Bolton, A. S., Burles, S., & Moustakas, L. A. 2006, *ApJ*, **640**, 662  
 Wilson, M. L., Zabludoff, A. I., Ammons, S. M., et al. 2016, *ApJ*, **833**, 194  
 Wilson, M. L., Zabludoff, A. I., Keeton, C. R., et al. 2017, *ApJ*, **850**, 94  
 Wong, K. C., Ishida, T., Tamura, Y., et al. 2017a, *ApJL*, **843**, L35  
 Wong, K. C., Keeton, C. R., Williams, K. A., Momcheva, I. G., & Zabludoff, A. I. 2011, *ApJ*, **726**, 84  
 Wong, K. C., Suyu, S. H., Auger, M. W., et al. 2017b, *MNRAS*, **465**, 4895  
 Xu, D., Sluse, D., Schneider, P., et al. 2016, *MNRAS*, **456**, 739  
 Zehavi, I., Zheng, Z., Weinberg, D. H., et al. 2005, *ApJ*, **630**, 1  
 Zhao, D. H., Jing, Y. P., Mo, H. J., & Börner, G. 2009, *ApJ*, **707**, 354